DNA-TR-85-333

AN EQUATORIAL SCINTILLATION MODEL

Edward J. Fremouw
Robert E. Robins
Physical Dynamics, Inc.
P. O. Box 3027
Bellevue, WA 98009-3027

DTIC
ELECTE
JUN 1 8 1986
S
D
D

30 September 1985

Technical Report

CONTRACT No. DNA 001-83-C-0097

Prepared for
    Director
    DEFENSE NUCLEAR AGENCY
    Washington, DC 20305-1000

86 6 17 107

DISTRIBUTION LIST UPDATE

This mailer is provided to enable DNA to maintain current distribution lists for reports. We would appreciate your providing the requested information.

☐ Add the individual listed to your distribution list.

☐ Delete the cited organization/individual.

☐ Change of address.

NAME: _____ _____

ORGANIZATION: _____ _____

OLD ADDRESS	**CURRENT ADDRESS**
_____	_____
_____	_____
_____	_____

TELEPHONE NUMBER: ( ) _____

SUBJECT AREA(s) OF INTEREST:

_____	_____
_____	_____
_____	_____

DNA OR OTHER GOVERNMENT CONTRACT NUMBER: _____

CERTIFICATION OF NEED-TO-KNOW BY GOVERNMENT SPONSOR (if other than DNA):

SPONSORING ORGANIZATION: _____

CONTRACTING OFFICER OR REPRESENTATIVE: _____

SIGNATURE: _____

AD-A168723

REPORT DOCUMENTATION PAGE	Form Approved OMB No 0704-0188 Exp Date Jun 30, 1986

1a REPORT SECURITY CLASSIFICATION UNCLASSIFIED	1b RESTRICTIVE MARKINGS

2a SECURITY CLASSIFICATION AUTHORITY N/A since Unclassified	3 DISTRIBUTION / AVAILABILITY OF REPORT
2b DECLASSIFICATION / DOWNGRADING SCHEDULE N/A since Unclassified	Approved for public release; distribution is unlimited.

4 PERFORMING ORGANIZATION REPORT NUMBER(S) PD-NW-85-342R	5 MONITORING ORGANIZATION REPORT NUMBER(S) DNA-TR-85-333

6a NAME OF PERFORMING ORGANIZATION Physical Dynamics, Inc.	6b OFFICE SYMBOL (If applicable)	7a NAME OF MONITORING ORGANIZATION Director Defense Nuclear Agency

6c ADDRESS (City, State, and ZIP Code) P.O. Box 3027 Bellevue, WA 98009-3027	7b ADDRESS (City, State, and ZIP Code) Washington, DC 20305-1000

8a NAME OF FUNDING / SPONSORING ORGANIZATION	8b OFFICE SYMBOL (If applicable)	9 PROCUREMENT INSTRUMENT IDENTIFICATION NUMBER DNA 001-83-C-0097

8c ADDRESS (City, State, and ZIP Code)	10 SOURCE OF FUNDING NUMBERS			
	PROGRAM ELEMENT NO 62715H	PROJECT NO I25AMXI	TASK NO 0	WORK UNIT ACCESSION NO DH006691

11 TITLE (Include Security Classification)

AN EQUATORIAL SCINTILLATION MODEL

12 PERSONAL AUTHOR(S)
Fremouw, Edward J. and Robins, Robert E.

13a TYPE OF REPORT Technical	13b TIME COVERED FROM 830201 TO 850430	14 DATE OF REPORT (Year, Month, Day) 850930	15 PAGE COUNT 74

16 SUPPLEMENTARY NOTATION
This work was sponsored by the Defense Nuclear Agency under RDT&E RMSS Code
B322085466 I25AMXI000082 H2590D.

17	COSATI CODES		18 SUBJECT TERMS (Continue on reverse if necessary and identify by block number)
FIELD	GROUP	SUB GROUP	Structured High-Altitude Plasmas Transionspheric Radio
20	9		Radiowave Scintillation and Radar Channels
18	3		Equatorial Scintillation

19 ABSTRACT (Continue on reverse if necessary and identify by block number)

Radiowave scintillation in the presence of natural and/or high-altitude nuclear disturbances has the potential to disrupt numerous transionospheric radio and radar systems. This report describes development of a model characterizing the plasma-density irregularities that produce scintillation in the naturally disturbed equatorial F layer. The model has been incorporated into Program WBMOD along with subroutines for computing both link geometry and scintillation indices, the latter by means of phase-screen diffraction theory. Earlier versions of WBMOD, which are operational at USAF Global Weather Central and at several other user locations, were based on extensive analysis of scintillation data collected in the auroral zone in DNA's Wideband Satellite Mission. The model described herein, which has been incorporated in WBMOD Version 8D1, is based on similarly extensive analysis of Wideband data from two equatorial stations. It describes irregularities at an effective height of 350 km that are isotropic across the geomagnetic field and elongated by a factor of 50 along the field and whose one-dimensional spatial power spectrum obeys a single-regime power law with

20 DISTRIBUTION / AVAILABILITY OF ABSTRACT ☐ UNCLASSIFIED/UNLIMITED ☒ SAME AS RPT ☐ DTIC USERS	21 ABSTRACT SECURITY CLASSIFICATION UNCLASSIFIED
22a NAME OF RESPONSIBLE INDIVIDUAL Betty L. Fox	22b TELEPHONE (Include Area Code) (202) 325-7042	22c OFFICE SYMBOL DNA/STTI

DD FORM 1473, 84 MAR

83 APR edition may be used until exhausted
All other editions are obsolete

19. ABSTRACT (Continued)

a (negative) spectral index of 1.5. The height-integrated spectral strength of the irregularities is modeled as a function of solar epoch (sunspot number), the angle between the sunset terminator and the geomagnetic field line through the equatorial F-layer point in question (a measure of seasonal and longitudinal variation), time after E-layer sunset on that field line, and the F-layer magnetic apex latitude of the point. The model does not include the secondary diurnal maximum in scintillation activity sometimes observed at equatorial stations nor the related variations in scintillation activity with geomagnetic disturbance level, which are considerably weaker than in the auroral zone. The report also highlights a factor missing from complete characterization of the joint seasonal/longitudinal variation of scintillation, thought to depend upon thermospheric neutral winds.

CONVERSION TABLE

Conversion factors for U.S. customary to metric (SI) units of measurement.

To Convert From	To	Multiply By
angstrom	meters (m)	1.000 000 X E -10
atmosphere (normal)	kilo pascal (kPa)	1.013 25　X E +2
bar	kilo pascal (kPa)	1 000 000 X E +2
barn	meter^2 (m^2)	1.000 000 X E -28
British thermal unit (thermochemical)	joule (J)	1.054 350 X E +3
calorie (thermochemical)	joule (J)	4.184 000
cal (thermochemical)/cm^2	mega joule/m^2 (MJ/m^2)	4.184 000 X E -2
curie	*giga becquerel (GBq)	3.700 000 X E +1
degree (angle)	radian (rad)	1.745 329 X E -2
degree Fahrenheit	degree kelvin (K)	$t_K = (t°f + 459.67)/1.8$
electron volt	joule (J)	1.602 19　X E -19
erg	joule (J)	1.000 000 X E -7
erg/second	watt (W)	1.000 000 X E -7
foot	meter (m)	3.048 000 X E -1
foot-pound-force	joule (J)	1.355 818
gallon (U.S liquid)	meter^3 (m^3)	3.785 412 X E -3
inch	meter (m)	2.540 000 X E -2
jerk	joule (J)	1 000 000 X E +9
joule/kilogram (J/kg) (radiation dose absorbed)	Gray (Gy)	1.000 000
kilotons	terajoules	4.183
kip (1000 lbf)	newton (N)	4.448 222 X E +3
kip/inch^2 (ksi)	kilo pascal (kPa)	6 894 757 X E +3
ktap	newton-second/m^2 (N-s/m^2)	1.000 000 X E +2
micron	meter (m)	1 000 000 X E -6
mil	meter (m)	2.540 000 X E -5
mile (international)	meter (m)	1.609 344 X E +3
ounce	kilogram (kg)	2.834 952 X E -2
pound-force (lbs avoirdupois)	newton (N)	4.448 222
pound-force inch	newton-meter (N·m)	1 129 848 X E -1
pound-force/inch	newton/meter (N/m)	1 751 268 X E +2
pound-force/foot^2	kilo pascal (kPa)	4 788 026 X E -2
pound-force/inch^2 (psi)	kilo pascal (kPa)	6.894 757
pound-mass (lbm avoirdupois)	kilogram (kg)	4 535 924 X E -1
pound-mass-foot^2 (moment of inertia)	kilogram-meter^2 (kg·m^2)	4 214 011 X E -2
pound-mass/foot^3	kilogram/meter^3 (kg/m^3)	1 601 846 X E +1
rad (radiation dose absorbed)	**Gray (Gy)	1 000 000 X E -2
roentgen	coulomb/kilogram (C/kg)	2 579 760 X E -4
shake	second (s)	1 000 000 X E -8
slug	kilogram (kg)	1.459 390 X E +1
torr (mm Hg, 0° C)	kilo pascal (kPa)	1 333 22　X E -1

*The becquerel (Bq) is the SI unit of radioactivity; 1 Bq - 1 event/s
**The Gray (Gy) is the SI unit of absorbed radiation

TABLE OF CONTENTS

LIST OF ILLUSTRATIONS

LIST OF TABLES

SECTION 1

INTRODUCTION

1.1 BACKGROUND

Research in the DNA community on the behavior of high-altitude plasma and its interaction with radio waves has led to a number of computer codes describing systems effects of both the ambient and the nuclear-disturbed ionosphere. In recent years, emphasis has been on structured plasmas, and a resulting code, WBMOD, for describing ambient radiowave scintillation has been placed in operation at USAF Global Weather Central and elsewhere.

Only now is high-altitude plasma structure being well characterized in the polar regions, by means of DNA's HiLat Satellite (Fremouw, 1983). Excluding these regions, it is well known that the latitude belts in which the strongest and most prevalent scintillation-producing structure occurs lie coincident with and just equatorward of the auroral oval and within about twenty degrees of the geomagnetic equator. The auroral scintillation model in WBMOD (Fremouw and Lansinger, 1981; Secan and Fremouw, 1983a) is based on extensive analysis of data from DNA's Wideband Satellite (Rino et al, 1977; Fremouw et al, 1978). This report presents a similarly based model of equatorial scintillation, which now also has been incorporated in WBMOD.

The code computes intensity and phase scintillation indices by means of the phase-screen scattering theory of Rino (1979a), the former corrected for multiple-scatter effects on the basis of Nakagami-Rice signal statistics (Fremouw and Miller, 1978). Its irregularity model characterizes the gradient sharpness, three-dimensional configuration, effective F-layer height, and height-integrated strength of structure represented by an anisotropic power-law spatial spectrum. In the auroral region, the strength is modeled as the product of separable functions of geomagnetic apex latitude, local magnetic (dipole) time, smoothed sunspot number, and planetary magnetic activity index, K_p. Irregularity motion there is described as the $\vec{E} \times \vec{B}$ drift driven by the high-latitude convection electric field, as modeled by Heelis et al (1982).

The dynamics of irregularity production in the equatorial F layer are thought to be simpler than those in the auroral and polar regions because there are fewer sources of ionization and free energy. It has turned out, however, that morphological characterization of the irregularities and their resulting scintillations is not any

1

easier at equatorial than at auroral latitudes. In part, this difficulty stems from the still enigmatic combination of seasonal and longitudinal variation in scintillation strength and occurrence, in spite of strides made in recent years toward its characterization and explanation (e.g., Tsunoda, 1985). It stems also, however, from data-base limitations.

There are many sources of semi-quantitative information about equatorial scintillation, but only one extensive and truly quantitative data base of high quality, namely that from Wideband. Unfortunately, the utility of that data base turned out to be less complete for equatorial scintillation than for the auroral zone for two main reasons. The first stems from Wideband's sun-synchronous orbit, which put a considerably more stringent local-time constraint on equatorial observations than on high-latitude ones. At ground stations near the equator only two or three passes could be observed in a twelve-hour period, all nighttime ones occurring at or after the pre-midnight scintillation maximum. At stations nearer the pole, such as Poker Flat, AK, several passes of Wideband in its hundred-degree-inclination orbit could be observed during a similar length of time, with F-layer penetration points being at different local times.

Secondly, observations at Poker Flat were essentially continuous during Wideband's nearly three-year lifetime, whereas those at the two equatorial stations, Ancon, Peru, and Kwajalein, Marshall Islands, were seasonally intermittent. Nonetheless, the high quality and extensive nature of the Wideband data base, particularly of phase scintillation, have made it possible for the first time to perform truly quantitative modeling of equatorial scintillation-producing irregularities. The manner in which this data base has been used is described in Section 2.2.

Equatorial scintillation has been known for many years to be primarily a nighttime phenomenon (Koster, 1958), although not quite exclusively (Rastogi and Mullen, 1981), and to increase with increasing solar activity during its eleven-year cycle (Paulson, 1979). It is also known to vary seasonally, the seasonal pattern being different in different longitude sectors (Koster, 1968; Moorthy et al, 1979; Basu et al, 1980; Paulson, 1981). Moreover, the Atlantic sector is known to be a site of particularly severe scintillation (Christiansen, 1971; Mullen et al, 1984). While auroral-zone scintillation increases in a relatively simple manner with increasing magnetic activity (Fremouw and Lansinger, 1981), the relationship between equatorial scintillation and magnetic activity is weaker and more complex (Koster and Wright, 1960; Aarons et al, 1980).

2

At any latitude, a scintillation model useful for applications must include a separation of those factors that control the geometry dependence of signal disruption and those that are of purely geophysical origin in their occurrence morphology. It is necessary, therefore, to invoke propagation theory to handle the geometrical aspects of the problem. The manner in which we have done so in the present work is described in Section 2.2.

There are several parameters that control the geometrical dependence of scintillation. First and foremost, the anisotropy of the irregularities dictates the strength of the phase perturbation imposed on the passing radio wavefront per unit of plasma-density irregularity strength. Specifically, axial ratios of anisotropic irregularities can be estimated from the degree of geometrical enhancement of scintillation as the radio line of sight grazes near coincidence with an axis of elongation. For a given three-dimensional configuration of irregularities, the ratio of the intensity scintillation index to the imposed phase perturbation depends upon the height of the irregularities through the Fresnel diffraction process.

There is a straightforward relationship between the temporal spectrum of measured phase scintillation and the spatial spectrum of the irregular structures that produce it. Thus, for power-law spectra, the phase spectrum may be used directly to deduce the *in-situ* spectral index that describes the size distribution of irregularities and the steepness of gradients associated with them. Once the effective height of the irregularities and their axial ratios and spectral index have been determined, one can invert phase-scintillation measurements directly via scattering theory to deduce the height-integrated strength of the irregularities.

The foregoing matters are elucidated in Section 2.2, where we present an idealized approach to scintillation analysis and modeling. Departures from the idealization, necessitated by data-quality limitations and other practicalities, are identified there and in Section 3, where we present our estimations and deductions of shape factors and height.

Shape and height are far less variable than is the strength of scintillation-producing irregularities, and we take the parameters characterizing them as constant. With this done, we present in Section 4 the main part of our work, development of an empirical, morphological model for the strength of scintillation-producing irregularities in the nighttime, equatorial F layer. In Section 4.1, we describe the particulars of that modeling process, which hinges upon separability of relationships with four independent variables. There and in Section 4.2 we address data-base

couplings between the various independent variables, which stem from nonuniform sampling. The latter also contains our main model results.

We attempt to characterize the efficacy of the model and its utility for computing representative and quasi worst-case scintillation indices in Section 5, in terms of statistical distributions. We conclude in Section 6 with a summary of the model and its applicability, including a discussion of outstanding questions about equatorial scintillation.

1.2 OBJECTIVE

The objective of the work carried out under this contract was to extend to equatorial latitudes the morphological efficacy and quantitative calibration of Program WBMOD that was carried out earlier for auroral latitudes. The purpose of the program is to provide a ready capability for computing intensity and phase scintillation indices for arbitrary transionospheric radio (one-way) and radar (two-way) systems operating at VHF and above, both for planning and for operational applications.

The primary outputs from WBMOD are the intensity scintillation index, S_4 (standard deviation of signal power, normalized to the mean power), and the phase scintillation indices, T (power spectral density of phase fluctuation at 1 Hz) and σ_ϕ (standard deviation of phase over a specified time interval). The code also outputs the power-law spectral index, p, of phase fluctuations to be expected during scintillation, but does not provide other second-order statistical moments such as temporal, spatial, or spectral correlation parameters.

SECTION 2

METHOD

2.1 WIDEBAND DATA

The DNA Wideband Satellite (P76-5) was launched in 1976 specifically for the purpose of diagnosing the scintillation-producing transionospheric communication channel. Its sole payload, a ten-frequency coherent radio beacon, operated continuously through February 1979. The beacon transmitted CW signals at S Band and L Band, a comb of seven equally spaced CW signals at UHF, and a CW signal at VHF. For the present work, we are concerned mainly with phase measurements made at VHF (138 MHz) using S Band (2891 MHz) as an essentially undisturbed phase reference.

As described by Fremouw et al (1978), the output of the VHF channel in the coherent receiver at a Wideband ground station consisted of two signals in phase quadrature with one another at the differential-doppler frequency imposed on the VHF/S-band pair of frequencies by the changing ionospheric path length as the line of sight scanned from horizon to horizon. These quadrature components were converted to intensity and phase records containing the scintillation information, as were the L-band (1239 MHz) and UHF (413±n·11.5 MHz) outputs. The differential doppler effect was removed by passing the phase record through a detrend filter with a cutoff of 10 sec.

The main observable employed in this work is the standard deviation of phase computed over the ten-second detrend period. Observations of significant interest in Wideband were spectrally analyzed, the resulting phase spectra undergoing a log-linear best fit and being characterized in terms of their power-law slope (spectral index) and strength. The latter, defined as the power spectral density (psd) at 1 Hz, is directly relatable to irregularity parameters through propagation theory, as will be summarized in Section 2.2. The variance of phase being the integral of the spectrum, we could relate our prime observable, which is the square root of the variance, to the irregularity parameters of interest for modeling, as also will be summarized there.

There were three Wideband receivers. The first was situated at Poker Flat, AK, for observations of auroral scintillation. The other two were used primarily for equatorial observations, the subject of this modeling effort. From the beginning of the experiment, a receiver was located at Ancon, Peru (11° 47' south, 77° 9' west, 0.4° north magnetic dip latitude). Initially, the third receiver was located at

Stanford, CA, for observations of the relatively undisturbed midlatitude ionosphere. It was moved to Kwajalein atoll in the Marshall Islands (9° 24' north, 167° 28' east, 4.4° north magnetic dip latitude) in October 1976 to provide a second equatorial station, primarily to observe longitudinal differences in equatorial scintillation. The total processed data base from Ancon consists of 347 nighttime and 137 daytime passes, typically containing about thirty twenty-second data-point sets, and that from Kwajalein consists of 363 nighttime passes and 169 daytime passes.

Observations at Poker Flat were virtually continuous through Wideband's operational lifetime, and the initial intent was to obtain similarly continuous equatorial observations. After approximately the first year, however, cost considerations lead to intermittent operation of the two equatorial stations, each being operated mainly during its then-perceived peak season. This has complicated identification of the true seasonal variation of scintillation activity at the two stations, and the manner with which we have dealt with this situation is described in Section 4.2.2.

In making use of Wideband data, we routinely employed data-editing procedures for safeguarding against interference, dead receiver channels, and the like. These procedures were adequate for data from Poker Flat, but the data from Ancon and Kwajalein turned out to have other problems. Inconsistencies in header formats over the experiment's lifetime required hand replacement of that information. Moreover, numerous overflow symbols and unreadable words required manual response. A recurring problem was erroneous azimuth and elevation values, stemming apparently from either shaft-encoder or A/D converter malfunction. These errors were identified by means of software that searched for out-of-range values and abrupt jumps, and then they were corrected by interpolation.

The most serious problem found in the data base resulted from cycle slips that had arisen in the conversion from quadrature components to intensity and phase. We attempted to correct for the problem in our modeling data base by scaling σ_ϕ from a higher frequency when significant cycle slipping was suspected. We did so by computing ratios of σ_ϕ measured at VHF, UHF, and L Band and comparing the results with the theoretically expected ratios. If two frequencies fell within specified bounds and the third did not, we flagged the third frequency as suspect. For modeling, we then replaced the suspected VHF values with theoretically scaled UHF values, when possible.

Figure 1a contains a scatter plot of VHF values of σ_ϕ, scaled from UHF if necessary and possible, against L-band values of σ_ϕ. The central broken line indicates the theoretically expected scaling law, and the other two represent our

6
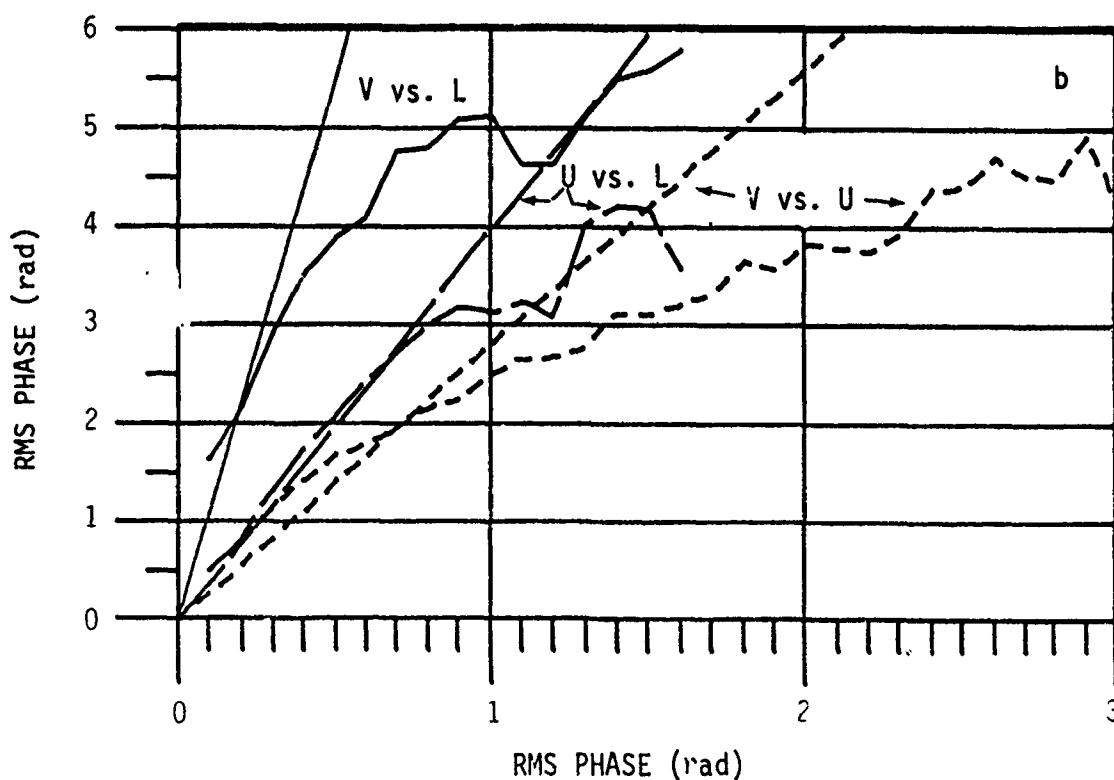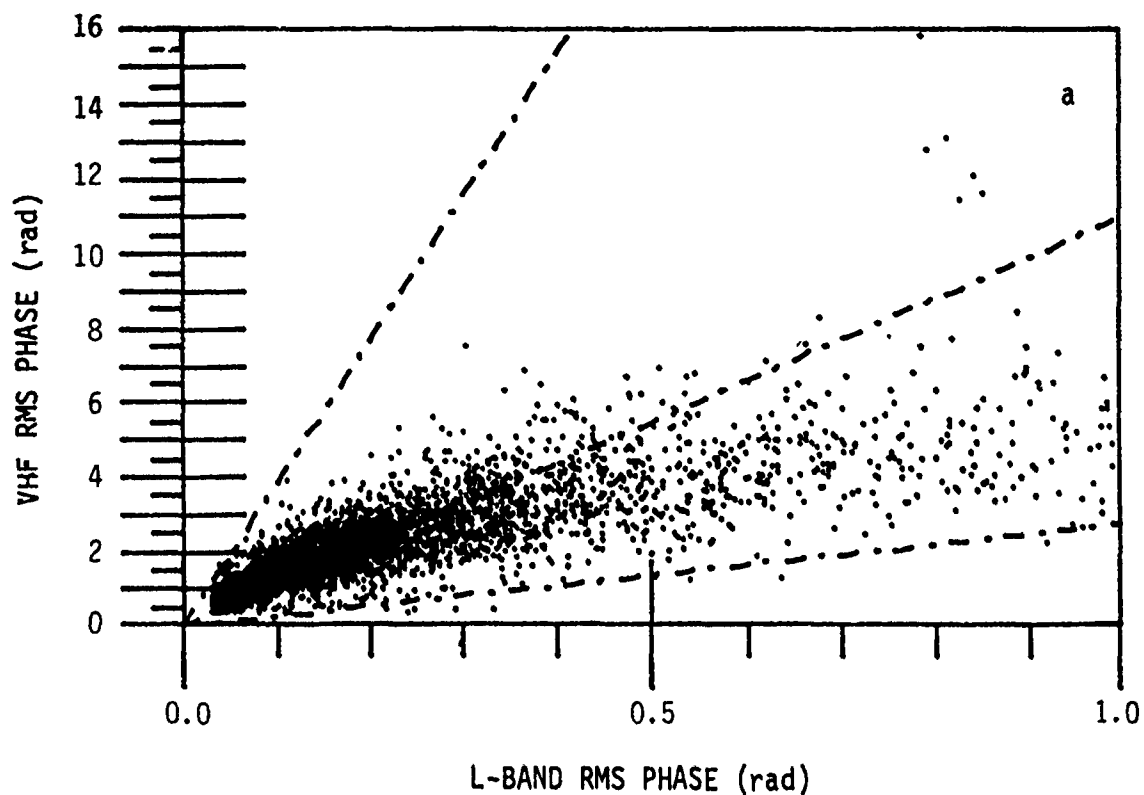
Figure 1. Frequency dependence of σ_ϕ on Wideband summary tapes from Kwajalein. (a) VHF values, scaled from UHF if frequency dependence strayed with certainty from theoretical expectation outside bounds shown (see text), plotted against L-band values. (b) Two-frequency average values, as indicated, compared with theoretically expected dependence (corresponding straight lines).

allowed departures from the expected ratio. (The few points outside the lower bound are cases in which UHF was not available for scaling.) The curvature in the scatter plot, systematically depressing it below the theoretically expected line, resulted mainly from cycle slipping, although there may have been some contribution from diffraction.

Figure 1b, which contains average curves drawn through two-frequency scatter plots of (non-scaled) σ_ϕ, indicates that cycle slipping (and, conceivably, diffraction) became a problem at UHF as well as at VHF for a σ_ϕ value of about three radians. Because a large majority of the measurements resulted in σ_ϕ values less than three radians, even at VHF, the direct effect of cycle slipping on the irregularity-strength model in WBMOD was acceptably slight. We shall see in Section 3.3, however, that it did complicate determination of the *in-situ* spectral index.

2.2 OVERVIEW OF PROCEDURE

The key to scintillation modeling, separation of geometrical from geophysical factors in control of the signal fluctuations experienced on a transionospheric communication (or radar) link, hinges on application of diffractive scatter theory. For this work, we made use of the phase-screen scattering theory of Rino (1979a) in two ways. The theory is employed directly in WBMOD, specifically in Subroutine SCINT3, to calculate scintillation indices from the irregularity model contained in Subroutine MDLPRM. Secondly, we have inverted that use to deduce irregularity parameters from scintillation observables, primarily the rms fluctuation of VHF phase, recorded in the Wideband experiment.

In the direct application of Rino's infinite outer-scale formulation of the theory, the central quantity calculated is T, the psd of phase at a fluctuation frequency of 1 Hz. It is given by

$$T = \lambda^2 r_e^2 \frac{\sqrt{\pi}\, \Gamma\left(\frac{q+1}{2}\right)}{(2\pi)^{(q+2)}\Gamma\left(\frac{q+2}{2}\right)} C_s L(\sec\theta)G\, V_e^q \tag{1}$$

where λ = radio wavelength,

r_e = classical electron radius,

θ = incidence angle of the propagation vector on the (horizontal) scattering layer.

The gamma functions arise from normalizing the three-dimensional ionospheric spectrum to the electron-density variance, $\left\langle (\Delta N)^2 \right\rangle$, such that

$$C_s = 8\pi^{3/2} \frac{\Gamma\left(\frac{q+2}{2}\right)}{\Gamma\left(\frac{q-1}{2}\right)} \frac{\langle(\Delta N)^2\rangle}{\alpha^{(q-1)}} \tag{2}$$

which is (to within a factor, ab, which is defined below and which Rino chose to incorporate in the geometrical factor, G) numerically equal to the strength of the three-dimensional spectrum at a (nonisotropic) wave number, K, of 1 rad/m. The spectrum itself is taken to be of the form $C_s K^{-n}$ in the spectral regime responsible for scintillation, but to be held finite by an outer scale, α. The gamma-function arguments depend only upon the sharpness of electron-density gradients, as expressed by the (one-dimensional) spectral index, q, given by

$$q = n-2. \tag{3}$$

The corresponding two-dimensional (phase) spectral index is (Cronyn, 1970)

$$p = q + 1. \tag{4}$$

The height-integrated spectral strength of the irregularities, $C_s L$, is contained in WBMOD's Function CSL, and our model for it in the equatorial region will be described in detail in Section 4. Conceptually, C_s is a structure constant characterizing the irregularity strength, and L is the (vertical) thickness of the irregular layer, but it is their product that is modeled from scintillation data.

The two remaining quantities in Eq. (1), G and V_e, describe respectively the static and dynamic aspects of geometrical control over phase scintillation. They are calculated in Subroutine GEOFAC, which is called by SCINT3, as follows:

$$G = \frac{a\,b}{\sqrt{AC - B^2/4}\,\cos\theta} \tag{5}$$

and

$$V_e = \frac{(CV_{sx}^2 - BV_{sx}V_{sy} + AV_{sy}^2)^{\frac{1}{2}}}{\sqrt{AC - B^2/4}} \tag{6}$$

where a = field-aligned axial ratio (ratio of irregularity size along the geomagnetic field to that normal to the field in a reference direction),

b = second axial ratio for describing sheetlike irregularities (ratio of irregularity size in direction normal to both the geomagnetic field and the reference direction to that in the reference direction),

and $\vec{V}_s$ = the foreshortened horizontal scan velocity of the line of sight, calculated in Subroutine VXYZ and defined in Eq. (14) of Rino (1979a).

The geometrical factors, A, B, and C, which are defined in Eq. (41) of Rino and Fremouw (1977), depend upon the incidence angle, θ, and magnetic heading, $\emptyset$, of the propagation vector, in addition to a and b. They depend also on the geomagnetic dip angle, ψ, and on a final irregularity parameter, δ, which is the angle that sets the reference direction for defining b.

The physical fact accounted for by the static geometrical enhancement factor, G, is that the phase perturbation imposed on a radio wave propagating along an extended dimension of irregularities builds up quasi-coherently, as compared with that for propagation along a short dimension. The description of this fact depends upon the propagation direction defined by θ and ϕ, the anisotropy of the irregularities defined by a and b, and the orientation of the irregularities defined by ψ and δ. The physical fact described by the effective velocity, V_e, is that a low-pass spatial spectrum results in stronger spectral density at a given temporal frequency (1 Hz) not only for greater scan velocities, but also for scans across short irregularity dimensions as compared with long ones. Thus, V_e depends not only on $\vec{V}_s$ but also on θ, ϕ, ψ and a, b, δ.

The fundamental outputs from WBMOD are T and p, which respectively are measures of the strength and spectral character of phase scintillation. The power-law spectral index, p, of phase is obtained from Eq. (4), which ignores the effect of diffraction on the shape of the phase spectrum. Diffractive alteration of p is believed to occur, but to be slight (Livingston *et al*, 1981), and the state of scintillation theory does not permit its calculation in general. As we shall see in Section 3.3, we have modeled q (and, therefore, p) as a constant because it is much less variable than the irregularity strength, C_sL, and because little is known about its variability. The code is structured so that future research results about spectral index could be incorporated in Subroutine MDLPRM. At present, WBMOD employs a value of 1.5 for q and outputs the corresponding value of p (2.5).

Unlike p, the strength, T, of phase scintillation is highly variable. The large majority of WBMOD is given over to calculating T and two commonly used indices of scintillation activity based on it, one for phase and one for intensity. The scintillation index for phase is simply its standard deviation, σ_ϕ, which may be calculated by integrating the phase-scintillation temporal spectrum, $\Phi_\phi(\nu)$, as follows:

$$\sigma_\phi^2 = 2 \int_{\nu_c}^{\infty} \phi_\phi(\nu) d\nu = 2 \int_{\nu_c}^{\infty} \frac{T \, d\nu}{(\nu_0^2 + \nu^2)^{p/2}} \tag{7}$$

where

$$\nu_0 = V_e/2\pi \, \alpha \, . \tag{8}$$

The outer scale, α, is measured in rad/m in the field-normal reference direction used in defining a and b, at the $2^{-q/2}$-point on the *in-situ* power spectrum.

In Eq. (7), ν_c is the lowest phase-fluctuation frequency to which the user's system is sensitive. For instance, in the Wideband experiment with normal processing, ν_c was 0.1 Hz, as set by phase detrending. In a coherently integrating radar, it would be the reciprocal of the time over which phase coherence is required. For systems not sensitive to phase instability produced in the propagation medium, ν_c is effectively infinite, and the effective σ_ϕ is zero.

Equation (7) may be evaluated for three ranges of the ratio, ν_c/ν_0, as follows:

$$\sigma_\phi^2 \begin{cases} \approx \dfrac{2 T \nu_c^{(1-p)}}{(p-1)} \quad ; \quad \dfrac{\nu_c}{\nu_0} \gg 1 & (9a) \\[4mm] = T \nu_0^{(1-p)} \left\{ \dfrac{\Gamma\left(\frac{p}{2} - \frac{1}{4}\right)}{\Gamma\left(\frac{p}{2}\right)} - 2 \left(\dfrac{\nu_c}{\nu_0}\right) {}_2F_1\left[\frac{p}{2}, \frac{1}{2}; \frac{3}{2}; -\left(\dfrac{\nu_c}{\nu_0}\right)^2\right] \right\} ; \dfrac{\nu_c}{\nu_0} \lesssim 1 & (9b) \\[4mm] \approx \pi \dfrac{\Gamma\left(\frac{p}{2} - \frac{1}{4}\right)}{\Gamma\left(\frac{p}{2}\right)} T \nu_0^{(1-p)} \quad ; \quad \dfrac{\nu_c}{\nu_0} \ll 1 & (9c) \end{cases}$$

where ${}_2F_1$, is the Gaussian hypergeometric function. Unfortunately, an analytical evaluation of Eq. (7) has not been found in the range $\nu_c/\nu_0 \gtrsim 1$.

The ionospheric outer scale, α, is sufficiently large that Eq. (9a) is quite valid over the range of effective velocity, V_e, encountered in Wideband, and we have employed it in our modeling. Moreover, the magnitude and variational behavior of α are not known. While the outer scale appears to be quite large compared with the spatial windows of a number of ionospheric experiments, there is no assurance that Eq. (9a) is valid for all systems in all operating scenarios. Accordingly, SCINT3

11

contains an efficient means (Subroutine OSRTN and Function F) for numerically evaluating Eq. (7), so that the code is not restricted inherently to application in the infinite outer-scale limit.

We have established that Eq. (9a) overestimates σ_ϕ by no more than 0.1% for $\nu_c/\nu_0 \geq 20$. The ν_c/ν_0 ratio is calculated in SCINT3, and σ_ϕ is calculated directly from Eq. (9a) for ratio values greater than 20. For values of 20 or smaller, SCINT3 calls Subroutine OSRTN for numerical evaluation of Eq. (7). As a default value, α is set at a very large constant value (10^6 m), so Eq. (9a) is employed in any likely application. An option is provided for the user to override the default value should he want to investigate the effect of varying the outer scale.

The scintillation index for intensity is the ratio, S_4, of the standard deviation of received signal power to the mean received power (Briggs and Parkin, 1963). u.. ike σ_ϕ, its relation to T is set not by a system or ionospheric parameter, but by the diffraction process that gives rise to intensity scintillation. For weak to moderate levels of intensity scintillation, S_4^2 is very well approximated (Rino, 1979a; Fremouw, 1980) by

$$S_{4w}^2 = C(q) \; \frac{T}{v_e^q} \; \frac{F}{G} \; Z^{q/2} \tag{10}$$

where

$$C(q) \begin{cases} = \dfrac{-2^{3q/2} \, \pi^{q+3/2}}{\tfrac{1}{2} \cdot \left(\tfrac{q+1}{2}\right)} \; \dfrac{\cos \pi\left(\tfrac{q}{4}\right)}{\cos \pi\left(\tfrac{q+1}{2}\right)} & ; \; q \neq 2 \tag{11a} \\[3mm] = 16^{-3} & ; \; q = 2 \tag{11b} \end{cases}$$

$$F = \frac{a\,b}{\sqrt{A'' \; C''^{q+1}}} \; {}_2F_1\left(-\frac{q}{2}, \frac{1}{2}; \; 1; \; \frac{A''-C''}{A''}\right) \tag{12}$$

and

$$Z = \frac{\lambda z \sec \theta}{4\pi} \;. \tag{13}$$

In the foregoing, A" and C" are geometrical parameters derived from A, B, and C by means of a coordinate rotation (Rino, 1979a), and z is the effective "reduced height" (including correction for wave-front curvature and curved-earth geometry) of the irregularities.

The two geometrical enhancement factors, G and V_e, that appear in Eq. (1) divide out of Eq. (10). The Fresnel filter factor, F, behaves in a fashion similar to G, however, and intensity scintillation also undergoes a geometrical enhancement. Nontheless, it is a weaker enhancement than that experienced in phase scintillation, due to the difference in V_e-dependence. In addition to describing static geometrical enhancement, F accounts for the effect of diffraction, together with the Fresnel-zone parameter, Z.

Now, Eq. (10) is a weak-scintillation formula. For practical purposes, however, it may be generalized to include the well-known saturation of S_4 at unity by writing

$$S_4^2 = 1 - \exp(-S_{4w}^2) . \tag{14}$$

Equation (14) is exact for scintillating signals that obey Rice statistics. Use of it ignores some effects of geometrical-optics focusing, which can drive S_4 modestly above unity (to 1.3 in rare and isolated instances) and which subtly alter the signal statistics accompanying scintillation (Fremouw, Livingston, and Miller, 1980). While considerable progress has been made on multiple-scatter theory (Rumsey, 1975; Rino, 1979b), a fully general expression for S_4 (the saturation behavior of which would depend upon q) is not available. Comparison of the behavior of S_4 and σ_ϕ, as measured in the Wideband experiment, shows that Eq. (14) is quite adequate to represent the behavior of S_4 for presently identified applications of WBMOD, and it has been coded into SCINT3.

The scintillation theory sketched in the foregoing discussion is well worked out for one-way propagation. For phase scintillation, the adaptation to two-way propagation is trivial. The round-trip propagation time is short compared with all other relevant time scales. Thus, the radio wave encounters the same irregularities twice, which doubles the phase perturbation and therefore quadruples its variance, σ_ϕ^2, and power spectral density, T. Accordingly, when a user chooses two-way propagation, WBMOD multiplies Eq. (1) by 4 to obtain the value of T that is output and used in Eqs. (7, 9a, and 10). Single-scatter considerations lead to a simple adaptation of Eq. (10) for describing intensity scintillation in two-way propagation. The effective reduced range is calculated for a scattering geometry that accounts for an image source and scattering region (the ionosphere encountered on the downlink), as well as for scattering on the uplink. We employ Eq. (14) as a multiple-scatter correction for two-way as well as for one-way propagation.

The foregoing describes the direct use of propagation theory in WBMOD. For establishing irregularity parameters from scintillation observations, one must invoke the theory in different ways. Table 1 lays out an idealized procedure for doing so. Listed along the top are seven physical parameters, each (except $\vec{V}_d$) defined earlier in this section, that are needed to characterize the irregularities and their motion. Along the left are identified six observables that, in principal, can be obtained from a fully instrumented scintillation experiment such as Wideband. The observables and parameters are not independently related one to one, but the X's indicate an efficient procedure for relating the two sets of quantities. The order is not important, except that the irregularity strength should be the last quantity deduced, since it is believed to be by far the most variable of the parameters.

The order of analysis in Table 1 begins with identification of the horizontal vector drift velocity, $\vec{V}_d$, of the irregularities* from spaced-receiver (interferometer) observations of the complex-signal diffraction pattern as it moves across the ground-based observing plane. In the absence of definitive interferometer-based measurements of drift velocity, we assume that F-layer irregularities drift essentially with the bulk plasma velocity, and we invoke a characterization of incoherent-scatter measurements thereof for our equatorial model.

An efficient procedure involves dealing early with the question of anisotropy across the magnetic field. Usually, one can tell from inspection of an aggregate data base whether or not there is a geometrical enhancement attributable to sheet-like irregularities, by noting whether or not such an enhancement is extended as a line across the sky or is restricted to the region near the magnetic zenith (Fremouw et al, 1977, Rino et al, 1978). In most instances the latter is the case, and one can then set the cross-field axial ratio, b, to unity and the sheet orientation angle, δ (now immaterial), to some arbitrary value such as zero. If not, then b and δ must be obtained by means of careful analysis of either the two-dimensional spatial auto-correlation function, $\rho(x,y)$, measured on the ground or the two-dimensional angular configuration of the enhancement. In either case, the field-aligned axial ratio, a, can be determined from such interferometer measurements or enhancement analysis.

---

*To be subtracted from the earth-frame scan velocity of the line of sight to obtain $\vec{V}_s$, the scan velocity through the irregularities.

14

Table 1. An idealized order of analysis.

Physical Parameters

Observables	Interferometer Measurements	$\vec{V_d}$	δ	b	a	q	h	C_sL
	$\vec{V_d}$	X						
	$\rho(x,y)$		X	X	X			
	Geometrical Enhancement		X	X	X			
	p					X		
	S_4/σ_ϕ						X	
	σ_ϕ							X

Given spectral analysis of a reliable phase-scintillation data base, determination of the *in-situ* spectral index, q, should be the simplest part of the entire analysis procedure, taking advantage of the trivial relationship, Eq. (4), between it and the observed phase spectral index, p. As we shall see, the cycle slipping identified in Section 2.1 precluded such direct determination of q from the equatorial Wideband data base, but a reliable value was determined from the frequency dependence of the intensity scintillation index, S_4.

With the drift velocity and all shape factors (anisotropy and gradient sharpness) established, the effective height, h, and the height-integrated strength, C_sL, can be deduced by direct calculation. In particular, dividing Eq. (10) by Eq. (9a) shows that the ratio of the intensity and phase scintillation indices is independent of the strength and depends only on the known observing geometry, the unknown height, and parameters deduced or estimated in earlier steps. Using that ratio to establish the height, one may then compute C_sL directly from Eqs. (9a) and (1), all other parameters on their right-hand sides being established and their left-hand sides being observables.

In practice with the equatorial Wideband data base, we necessarily departed considerably from the idealized scheme represented by Table 1. Our actual procedure is outlined in Table 2, the elements of which are discussed in Sections 3 and 4.

16

Table 2. Order of analysis employed.

Physical Parameters

Observables	V_d	b	δ	q	h	a	$C_s L$
Incoherent Scatter	night:east 100 m/s day:west 50 m/s						
No Extended Enhancement		1	(0)				
$S_4(f)$				1.5			
$\sigma_\phi(lat)$					350 km		
S_4/σ_ϕ						50	
σ_ϕ							Model

SECTION 3

DRIFT, HEIGHT, AND SHAPE FACTORS

3.1 DRIFT VELOCITY

Our first departure from the idealized procedure outlined in Table 1 arose from the fact that little analysis has been performed on Wideband's interferometer data, but the departure probably is of little consequence. Specifically, we employed published incoherent-scatter data as a basis for modeling F-layer drift in the equatorial region. Because Wideband was in low orbit, we did not expect drift velocity to be an outcome of its interferometer measurements anyway, although Rino and Livingston (1982) were able to produce such estimates in selected cases.

In earlier work (Secan and Fremouw, 1983a), we introduced into WBMOD a geophysically based model (Heelis *et al*, 1982) to describe the convective drift of F-layer irregularities at high latitudes. Now we have introduced a similarly realistic but far simpler description of F-layer drift at equatorial latitudes. Based on extensive incoherent-scatter observations at Jicamarca (Fejer *et al*, 1981), it consists of the following diurnally cyclic variation, with eastward drifts reaching 100 m/s at about 2200 local time, westward drifts reaching 50 m/s at about 1000, and reversals taking place just after 1600 and 0400:

$$V_{dy} = 25 + 75 \sin\left[\frac{2\pi}{24}(t_e + 1.36)\right] \text{ m/s} \tag{15}$$

where t_e is time after E-layer sunset* in hours. The value 1.36 was chosen to place the May - August reversal exactly at 1600, as it appears in Figure 2 of Fejer *et al* (1981). A smooth transition is provided to a more nearly co-rotating pattern at middle latitudes.

We used t_e instead of local time primarily to maintain consistency with the time factor in the equatorial $\sqrt{C_s L}$ representation. (See Section 4.1 and 4.2.3.). It turned out, however, that using t_e also reproduced a subtlety in the observations of Fejer *et al* (1981), which would not have been obtained if local time had been used. Namely, the data in Figure 2 of Fejer *et al* (1981) show a shift in the westward-to-eastward reversal from exactly 1600 during May - August to between 1600 and 1700 during November - February. Use of t_e caused the above plasma-drift model to emulate this shift, whereas local time would have caused the reversal time to be constant.

---

*See Section 4.1 for a more complete definition of t_e.

18

3.2 CROSS-FIELD ISOTROPY

A more significant limitation of Wideband's interferometer measurements turned out to be that its maximum baseline of 900 meters was insufficient to record any decrease in signal correlation in the geomagnetic north-south direction at either of the equatorial stations. This result attests to the known fact (Koster *et al*, 1966) that equatorial irregularities are highly elongated along the magnetic field, but it precludes a quantitative measurement of axial ratios and orientation.

As indicated in Section 2.2, one can deduce the general configuration of the irregularities by noting the characteristics of geometric enhancement. Thus, aggregate enhancement along the L-shell passing from the F layer through Poker Flat (Fremouw *et al*, 1977) was interpreted (Rino *et al*, 1978) as the signature of sheetlike irregularities in the subauroral ionosphere. No such extended feature was apparent in the aggregate data bases from Ancon or Kwajalein, even though plasma "bubbles" and backscatter plumes are known to align themselves quasi-vertically with an eastward tilt. Lack of such a signature in aggregate scintillation data prompted us to model the crossfield axial ratio, b, as unity (as indicated in Table 2) and to set the (now inconsequential) orientation angle, δ, arbitrarily to zero (as indicated in parentheses in Table 2). That is, WBMOD describes equatorial irregularities as isotropic across the magnetic field.

Without interferometer measurements, one hopes to rely on a clear geometrical enhancement for establishing axial ratios. Given cross-field isotropy (b=1), any such enhancement should be confined to look angles for which the radio line of sight is nearly aligned with the magnetic field, and such enhancements are quite prominent at higher latitudes. For dip angles near zero, however, any such enhancement occurs near the northern and southern horizons, and it is difficult to separate it from enhancements due to increasing path length and from contamination by ground reflections. Accordingly, we postponed estimation of the along-field axial ratio, a, until we could invoke the theory with additional parameters already evaluated. We shall return to this point in Section 3.5.

3.3. SPECTRAL INDEX

Again, one should be able to employ the trivial relationship, Eq. (4), between the phase-scintillation spectral index, p, and that of the *in-situ* irregularities, q, to obtain the latter, and we had intended to do so at the outset of this work. Given a reasonably narrow distribution of p values, one could model q as a constant simply by subtracting unity from the mean, median, or most frequent value of p.

Figure 2 contains the statistical distribution of nighttime* p values for which scintillation was sufficiently strong for the phase spectrum to be of interest at Kwajalein and Ancon. The two data sets are very consistent, both showing a most frequent value of 2.3 (*in-situ* index, q, of 1.3) and a skewed distribution. The distribution is sufficiently broad, however, that one may reasonably inquire into trends in the spectral index.

Livingston *et al* (1981) reported decreasing p (and q) values with increasing scintillation severity in a moderate number of scintillation (and *in-situ*) measurements. Figure 3a, which is a scatter plot of almost four thousand VHF values of p measured at Kwajalein, shows that the behavior they reported is statistically very consistent. The solid and dashed lines on the figure demark respectively the mean values and standard deviation of p as a function of σ_ϕ. The mean-value curve is repeated in Figure 3b along with its counterpart from Ancon and similar UHF curves measured at the two stations. A best-fit straight line through the cluster of curves is as follows:

$$p = 1.7 - 0.14 \, \sigma_\phi.$$

The consistency between data from the two stations is reassuring, but the strict consistency between the curves from the two frequencies is disconcerting. Each of the ordinates in Figure 3b is plotted against a different abscissa, namely the value of σ_ϕ measured at the station and frequency at which p was measured. Thus, a given abscissa value represents different levels of ionospheric irregularity at the two frequencies. It appears that the downward slope exhibited in Figure 3 results more from diffraction and/or data-processing artifacts than from inherent ionospheric behavior.

The foregoing inference is corroborated by Figure 4, which presents phase spectral-index values measured at VHF and UHF against a common measure of ionospheric disturbance, namely σ_ϕ measured at VHF. The displacement between the two curves, representing more fine structure in the VHF fluctuations than in their UHF counterparts, clearly must result from propagation and/or a frequency-dependent experimental artifact. We attribute the down-turn in the UHF curve for very weak scintillation (VHF $\sigma_\phi \leq 1.3$ rad, which corresponds to a UHF σ_ϕ value of 0.5 rad) to noise contamination of the UHF spectrum.

---

*Distribution histograms of daytime and nighttime values of σ_ϕ and S_4 from both stations confirmed the expectation that daytime scintillation there is negligible at VHF, UHF, and L Band.
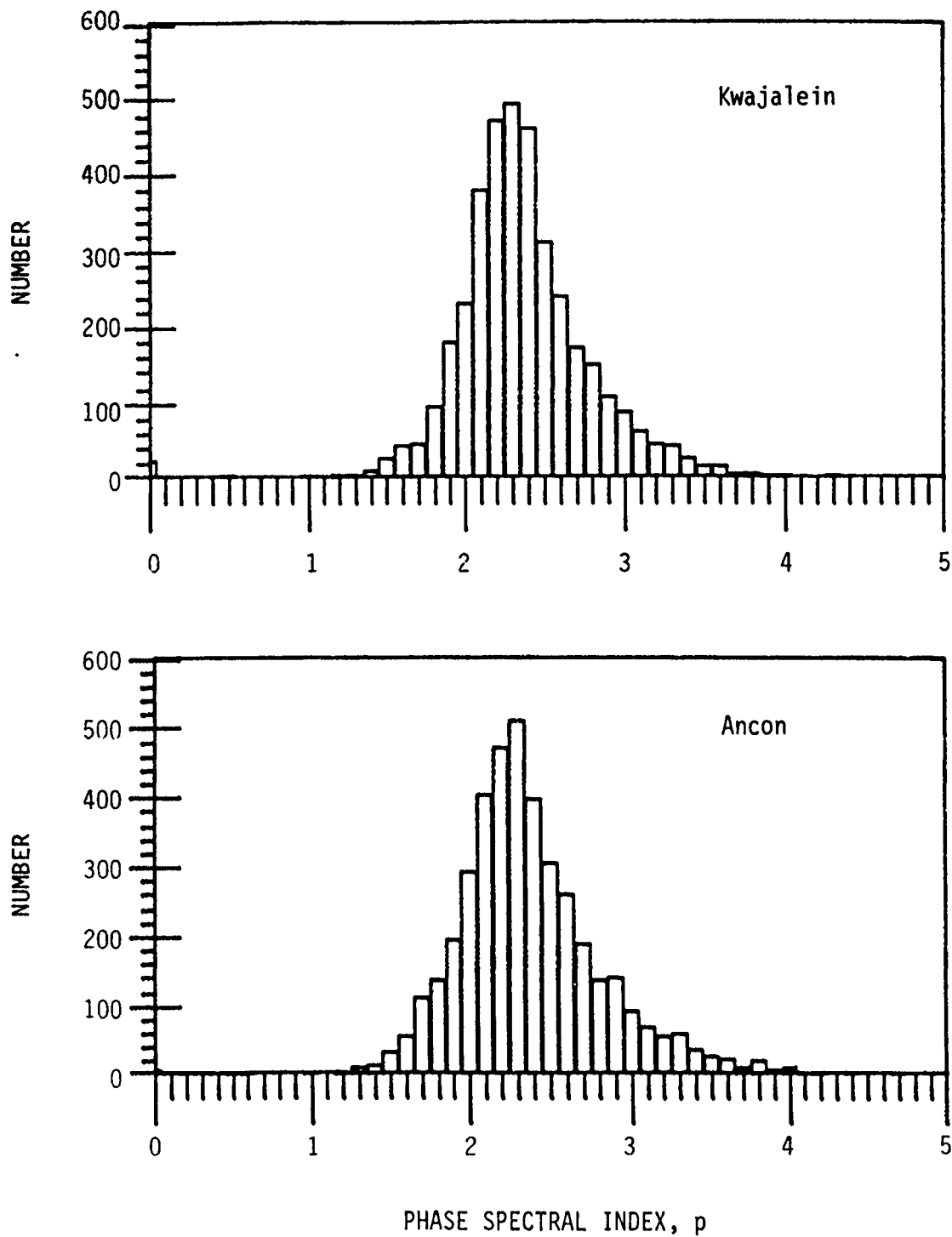
Figure 2. Occurrence distributions of the VHF (138 MHz) phase spectral index, p, measured in Wideband at night at the two equatorial stations.
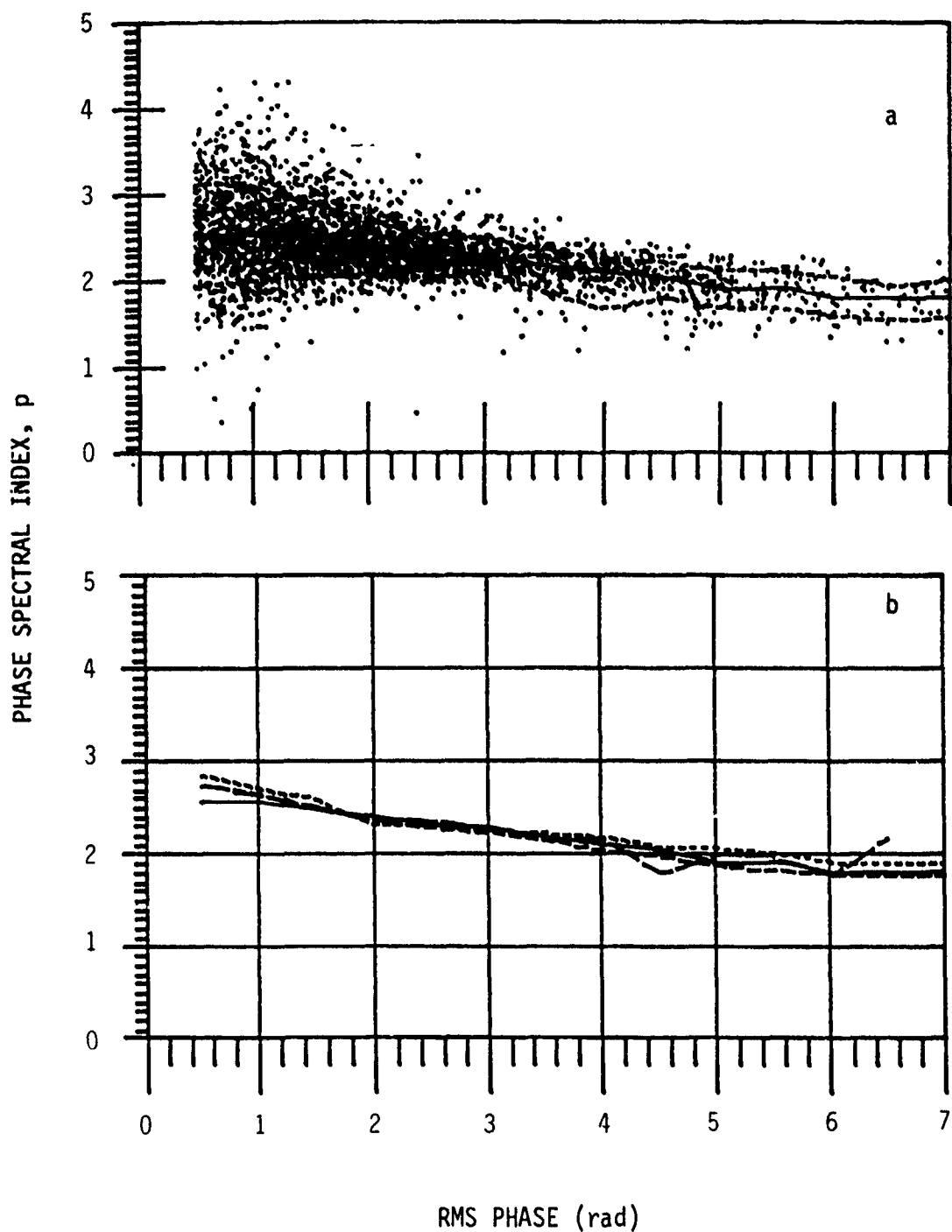
Figure 3.   Dependence of phase spectral index, p, on phase scintillation
index, σ_ϕ.   (a) VHF nighttime values measured at Kwajalein.
(b) Mean nighttime values measured at Kwajalein and Ancon at
VHF and UHF (379 MHz).
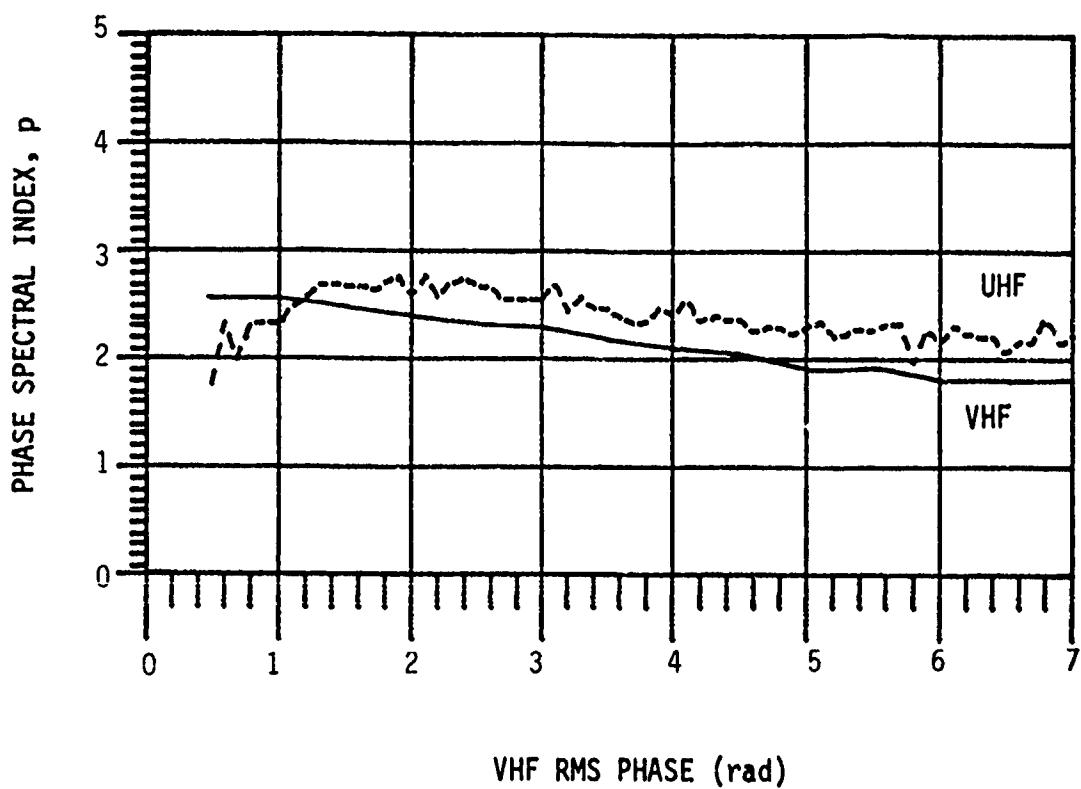
Figure 4. Average nighttime value of p measured at Kwajalein at VHF (solid) and UHF (broken) plotted against a common measure of ionospheric irregularity, the value of σ_ϕ measured at VHF.

As discussed in Section 2.1, cycle slips constitute a "frequency-dependent experimental artifact" in the Wideband phase data base. The upshot is that cycle slips probably caused Figures 3 and 4 to overstate the slope of the p dependence on scintillation strength. Moreover, they must have contaminated the spectra from which the p values were derived, probably introducing excess psd at the high-frequency end (i.e., reducing p). We must conclude that the decrease in measured p with increasing σ_ϕ noted in Figures 3 and 4 may not represent a decrease in the *in-situ* spectral index, q, at all.

Now, Livingston *et al* (1981) and Rino *et al* (1981) found the behavior in question not only in phase-scintillation data but also in *in-situ* data, which are inherently immune from cycle slipping. This fact would seem to establish the geophysical reality of the behavior. There is another artifact, however, that could have contaminated the *in-situ* spectra as well as the scintillation spectra, namely spectral leakage. Leakage contamination also would be in the sense to decrease the measured q values as the plasma-density perturbation increases. Livingston (private communication) has confirmed that the *in-situ* data were not windowed before being spectrally analyzed. Thus, they could have been contaminated by spectral leakage.

In view of the foregoing, we have not incorporated a dependence of q on irregularity strength in WBMOD. Rather, we have fixed q at the value most consistent with the frequency dependence of nonsaturated S_4 values measured at Ancon and Kwajalein, which turns out also to be the value used earlier in WBMOD's high-latitude description (Secan and Fremouw, 1983a). The basis for choosing the q value, 1.5, is illustrated in Figure 5, which is a plot of UHF vs L-band values of S_4 measured at Kwajalein.

Equation (10), in conjunction with (1) and (13), indicates that S_4 is proportional to $\lambda^{(1 + q/4)}$. Accordingly, in the weak-scatter regime,

$$q = 4 \left[\frac{\ln(S_{4f}/S_{4f'})}{\ln(f'/f)} - 1 \right] \tag{16}$$

where f and f' are two frequencies at which intensity scintillation indices of S_{4f} and $S_{4f'}$ are measured, respectively. A linear best fit to the mean curve in Figure 5 in the weak-scatter regime ($S_{4u} \leq 0.5$) revealed a slope of 5.06, which yields a q value of 1.47. The same procedure applied to a plot of S_{4v} vs S_{4u} showed a slope of 3.95, corresponding to a q of 1.48. Repeating the procedure with Ancon data yielded 1.52 for q. From the combined results, we fixed q at 1.5 in WBMOD.
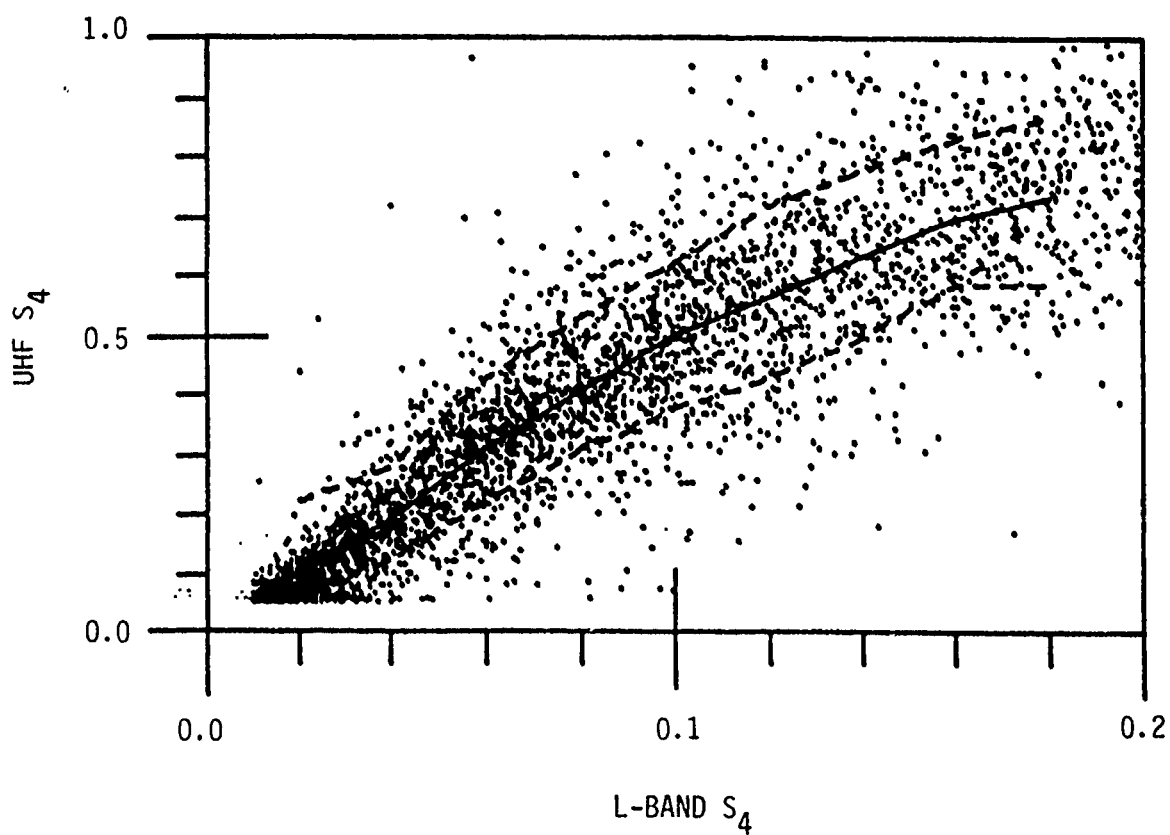
Figure 5.   Frequency dependence of non-saturated values of intensity scintillation index, S_4, measured at night at Kwajalein.

3.4 HEIGHT OF THE EQUIVALENT PHASE SCREEN

In the phase-screen representation of scintillation-producing irregularities, the presumably thick region of plasma-density structure is replaced by an equivalent phase-modulation pattern on a plane located near the centroid height of the region. This equivalent phase-modulating screen reproduces the complex-signal pattern observed at any subsequent observing plane, such as the ground.

At the screen, the signal perturbation is purely one of phase, and the ratio of intensity to phase scintillation index at the observing plane offers one means to estimate the height of the equivalent phase screen. We had intended to do so, but as we shall see in Section 3.5, we employed the index ratio instead to estimate the degree of field-aligned anisotropy of equatorial irregularities. That we were able to do so was fortunate, in view of unavailability of definitive spaced-receiver measurements and lack of a prominent geometric enhancement, as well as unexpected.

Our estimation of height stemmed essentially from the fact that the observing geometry (primarily viewing angles relative to the local geomagnetic field, along which the irregularities are elongated) changes with altitude. For a uniform or other simple and symmetrical distribution of irregularity strength with magnetic latitude, we found subtle differences in the computed distribution of phase scintillation strength with latitude for observations from Kwajalein, depending upon the height chosen for the irregularities.

Initially, we had set the height of the equatorial scintillation-producing phase screen at 500 km, based on the extent of irregularity plumes revealed by backscatter radars during severe scintillation conditions. To test other choices made early in our modeling effort, we selected nighttime data from three pass corridors over Kwajalein, one to the east of the station, one consisting of nearly overhead passes, and one to the west. Each corridor was 2° of longitude in width. After selecting values of appropriate model parameters to ensure a match to the mean scintillation level in each data corridor, we found that good fits to the latitudinal variation of phase scintillation strength were significantly better when the model height was changed from 500 to 350 km. Indeed, the 350-km fits, which are shown in Figure 6, are rather remarkable. Moreover, subsequent tests showed slightly poorer fits for 250 and 450 km.

The sensitivity of the observed latitudinal distribution of phase scintillation index to phase-screen height evidently stems primarily from sensitivity of V_e (with a
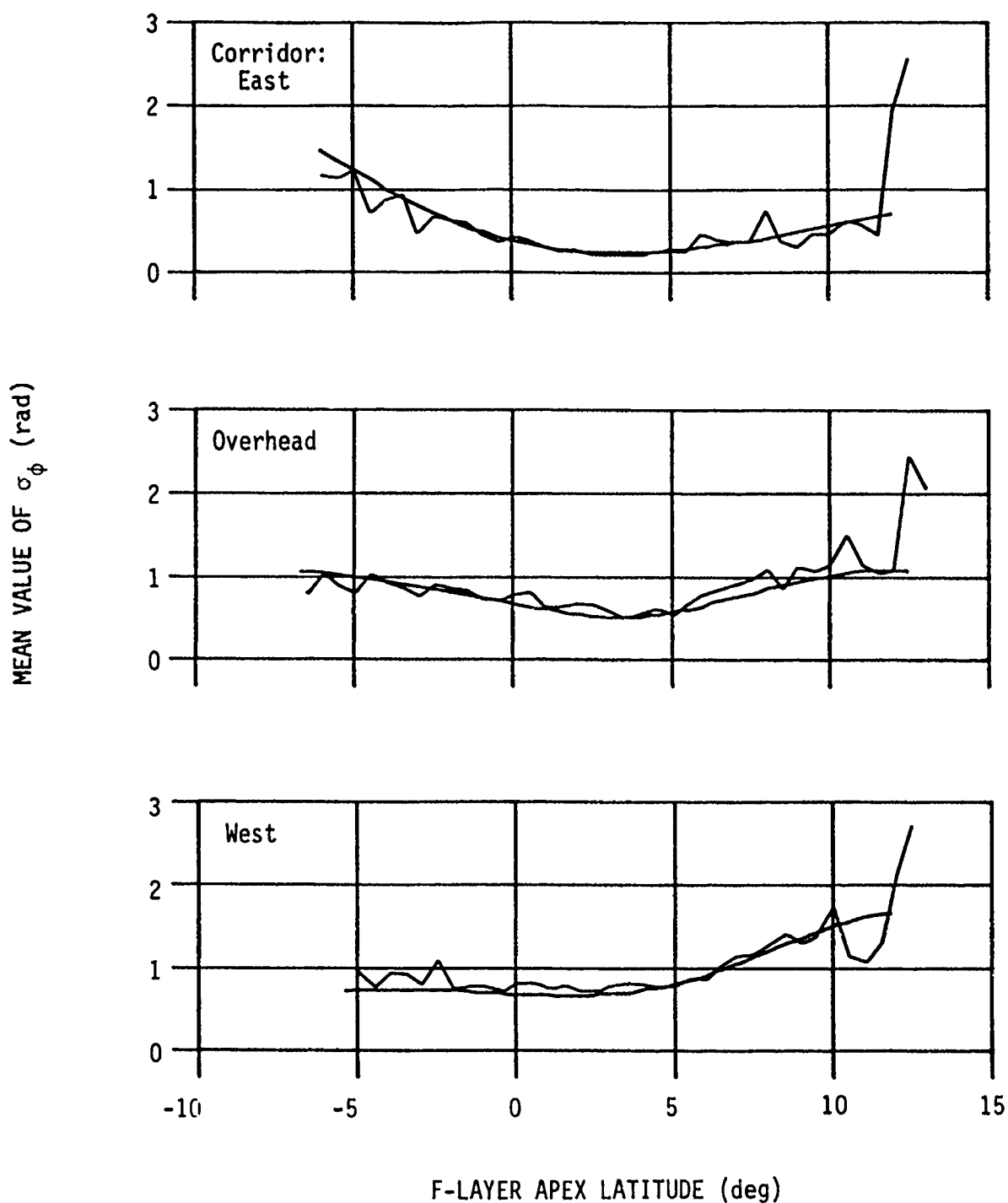
Figure 6. Comparison of WBMOD representation (smooth curves) of latitudinal dependence of equatorial phase scintillation at VHF (138 MHz) with mean dependence observed (irregular curves) at night from Kwajalein in the Wideband mission. Data population ranges from 25 to 80 measurements per half-degree latitude bin, and the data curves have been cut off where (in all corridors) the population drops abruptly from over 25 to less than 10 per bin.

possible secondary contribution from G) to the precise orientation of highly elongated irregularities, given Wideband's high-inclination orbit. Its reliable calculation arises from use of an accurate geomagnetic field model, as we verified by observing the effect of introducing small departures from the International Geomagnetic Reference Field.

Based on the foregoing, we have set the irregularity model's equatorial height at 350 km, as it also is at middle and high latitudes. A greater height may be appropriate for strong scintillation events dominated by plumes, but the aggregate scintillation data population is better characterized by a phase-screen height of 350 km. This probably stems from the contribution of bottomside spread-F irregularities to less severe but more frequent scintillation.

3.5 ALONG-FIELD AXIAL RATIO

Lack of evidence for cross-field anisotropy in equatorial irregularities (Section 3.2) reduced by two the number of model parameters needed. Moreover, as indicated in Section 3.4, an unexpected bonus allowed us to determine the effective height of the irregularities from the observed latitudinal dependence of phase scintillation strength in three longitudinal corridors near each of the two equatorial stations. Finally, as described in Section 3.3, we were able to determine the *in-situ* spectral index with considerable confidence from the frequency dependence of intensity scintillation. The foregoing leaves only the along-field axial ratio, a, and the height-integrated irregularity strength, C_sL, to be determined.

We employed both intensity and phase scintillation, specifically the ratio of their strengths, to determine a. Both S_4 and the strength of phase scintillation, whether measured by the standard deviation, σ_ϕ, or its spectral counterpart, T, depend upon C_sL. Their ratio, however, does not. Indeed, Equations (4), (9a), (10), and (14) show that, for weak scintillation ($S_4 \ll 1$),

$$\frac{S_4^2}{\sigma_\phi^2} = \frac{qC(q)}{2} \frac{F(a, \text{geometry})}{G(a, \text{geometry})} \frac{Z^{q/2} v_c^{-q}}{\left[V_e(a, \text{geometry})\right]^q} \tag{17}$$

Both Z and V_e increase linearly with increasing irregularity height, h. Given a reliable value for q, an estimate for h, and knowledge of all other aspects of the observing geometry, we were able to estimate a by means of Equation (17). Figure 7 contains plots of the scintillation-index ratio vs F-layer magnetic apex latitude for Wideband pass corridors to the east (top) and west (bottom) of Ancon. The solid curves
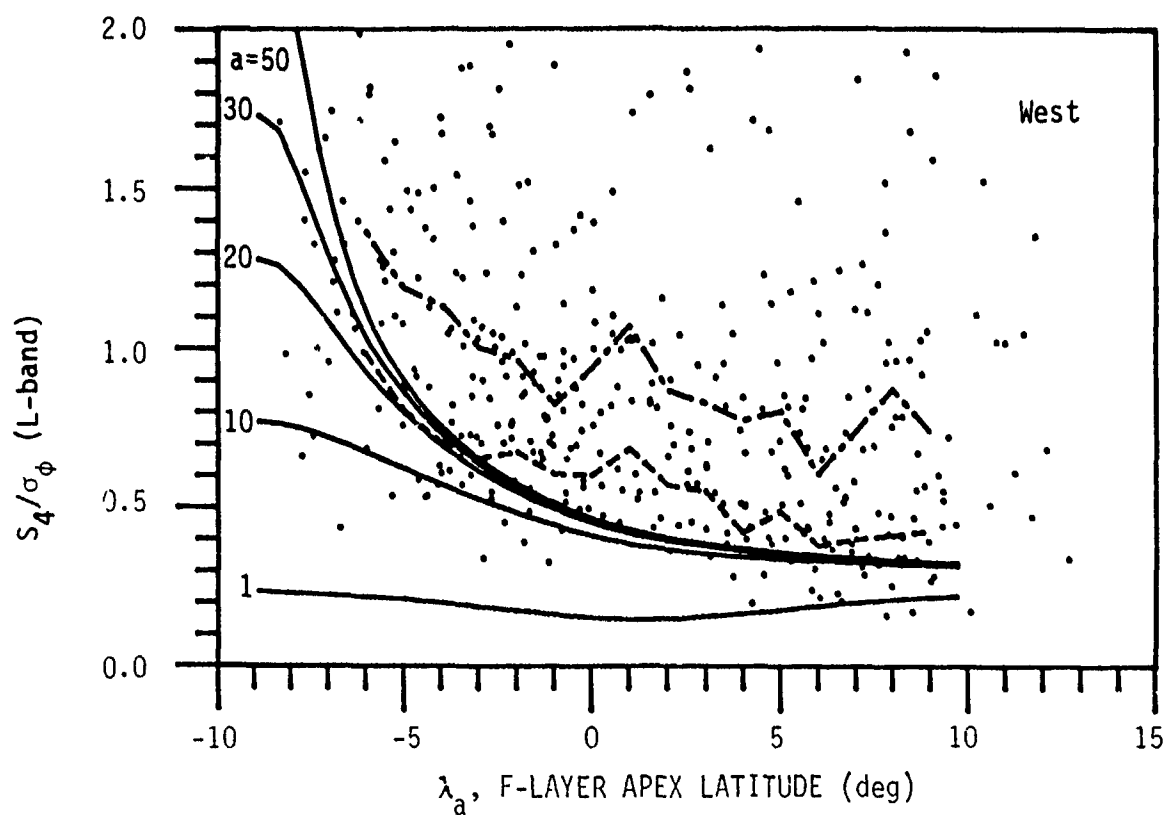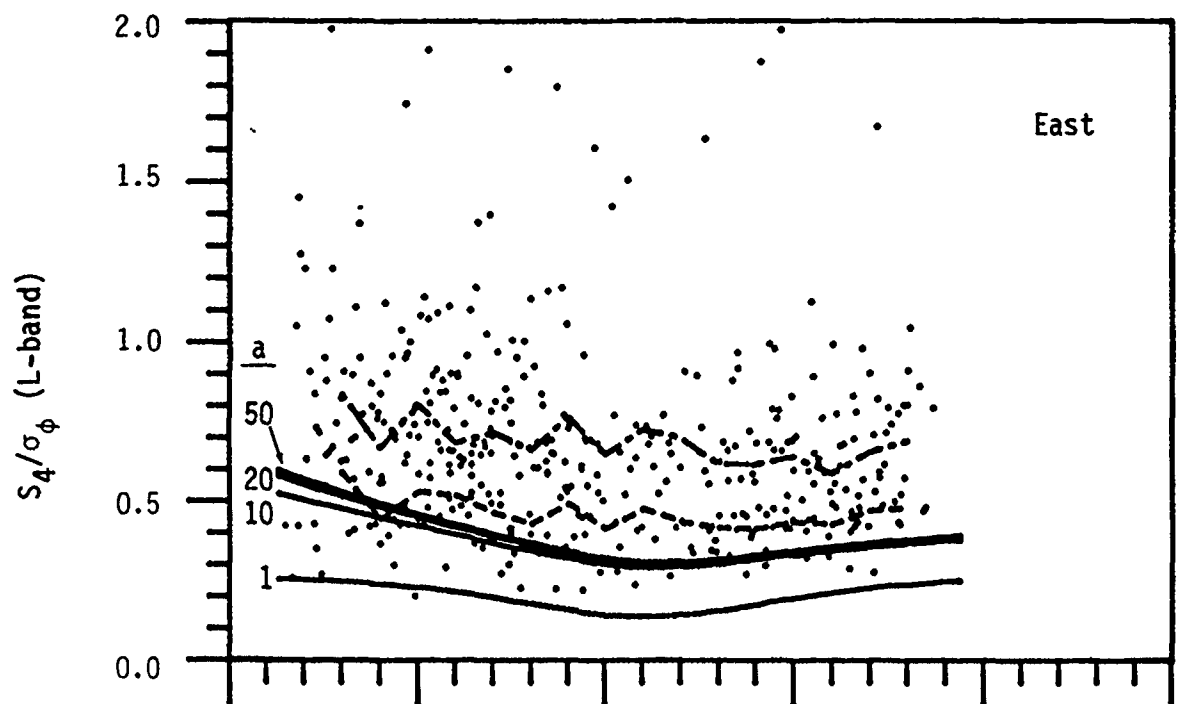
28

Figure 7. Scintillation-index ratio in Wideband pass corridors to east and west of Ancon. Broken curves: mean and lower standard deviation. Solid curves: computed for various field-aligned axial ratios, a.

29

were computed by WBMOD for different irregularity axial ratios and a fixed height (350 km), spectral index (1.5), and detrend cutoff (0.1 Hz).

On both plots, the scatter of dots represents the Wideband data base of individual L-band measurements. The L-band data base was used to avoid saturated values of S_4 without disciminating against well-developed scintillation conditions. The distribution of S_4/σ_ϕ measurements is quite skewed, with the bulk of the data points in all corridors lying between the mean and the lower standard deviation. These two moments are shown in Figure 7 by the dot-dash and dashed curves, respectively. Clearly, the vast majority of measured values is consistent with very elongated irregularites. Indeed, the bulk of the data corresponds to theoretically saturated values of axial ratio.

Equatorial irregularities may, indeed, be extremely elongated (a > 50, say, or even > 100). We take some guidance, however, from the fact that the mean and standard deviation curves (and the general pattern of points) do not rise more steeply toward the south of the west corridor than do the curves computed for a = 30 and a = 50. Combining our results, we chose a value of 50 for field-aligned axial ratio, a, to characterize the anisotropy of equatorial irregularities (along with a cross-field axial ratio, b, of unity). We note that truly definitive measurements of axial ratio near the equator have yet to be made, but that the precise axial ratio is of little consequence for most applications in regions of low geomagnetic dip. For most applications, it is sufficient simply to employ a >> 1.

SECTION 4

IRREGULARITY STRENGTH MODEL

4.1 PROCEDURE

In the previous sections we have described the determination of all parameters in the equatorial scintillation model except for C_sL, the height-integrated spectral strength of irregularities. We present in this section our procedures for obtaining a representation for C_sL, followed by the results.

Our basic assumption regarding C_sL is that it can be represented in terms of the following influences: solar activity, magnetic latitude, a combination of season and longitude, and some measure of local time. Prior to the work reported herein, WBMOD characterized these influences in terms of variables as follows:

INFLUENCE	VARIABLE
solar activity	$\bar{R}$, smoothed Zurich sunspot number
magnetic latitude	λ_d, dip latitude
season/longitude	D, day of year
	λ_g, geographic latitude
	Δ_d, a phase delay (days) in the day-of-year dependence, depending on location
local time	t, local geographic-meridian time (hours)

The actual quantity estimated by WBMOD is $\sqrt{C_sL}$, where it was assumed that

$$\sqrt{C_sL} = C_E f_R(\bar{R}) f_L(\lambda_d) f_S(D, \lambda_g, \Delta_d) f_T(t), \tag{18}$$

i.e., that the various influences could be represented as separable factors. Here, C_E is a lead constant. The actual forms for the functions f_R, f_L, f_S, f_T are given by Secan and Fremouw (1983a), but are not important for the present discussion.

In the updated version of WBMOD, we retain the same influences and basic functional form for $\sqrt{C_sL}$, but we introduce new variables, except for $\bar{R}$. These are briefly described in the following table, with more complete descriptions below.

31

OLD VARIABLE	NEW VARIABLE
λ_d	λ_a, apex latitude
$\left.\begin{array}{l} D \\ \lambda_g \\ \Delta_d^g \end{array}\right\}$	τ, angle between solar terminator and magnetic meridian, at geomagnetic equator
t	t_e, time after E-layer sunset

Apex latitude, λ_a, was adopted so that WBMOD could use the same latitude coordinate for polar, mid-latitude, and equatorial regions. Previously, invariant latitude was used poleward of the plasmapause, and dip latitude was used near the dip equator. The definition and use of apex latitude is described by Van Zandt, et al (1972) and our adaptation of it by Secan and Fremouw (1983b).

Use of the variables τ and t_e was motivated by the Tsunoda-Wittwer postulate (Tsunoda, 1985), which states that scintillation-producing irregularities are most likely to develop in the equatorial F-layer when the integrated E-region Pederson conductivity experiences its maximum longitudinal gradient. One consequence of this postulate is that scintillation activity should maximize, at a given longitude, during the season in which the solar terminator is most nearly aligned with the geomagnetic field lines passing through that longitude. For a given F-layer penetration point, τ is defined as the angle between the solar terminator and the geomagnetic meridian at the point where the geomagnetic field line through the F-layer penetration point intersects the geomagnetic equatorial plane. Thus, the condition $\tau = 0$ is very nearly equivalent to the Tsunoda-Wittwer criterion for the season in which scintillation activity should maximize.

The definition of t_e is in terms of when the sun sets at the two intersection points between the geomagnetic field line through the F-layer penetration point and the E layer. Specifically, it is the time (hours) after the later sunset at these two E-layer locations.* According to the physics underlying the Tsunoda-Wittwer postulate, it is only after this "dual sunset" that scintillation is likely to occur. Another statement of the criterion for the season in which scintillation is most likely to occur is that these two sunsets be simultaneous.

Assuming the basic representation,

$$\sqrt{C_s L} = C_e \, f_r(\bar{R}) f_s(\tau) f_t(t_e) f_\lambda(\lambda_a), \tag{19}$$

---

*For consistency, t_e was used instead of t also in Equation (15), the expression for equatorial drift velocity.

we proceeded to use the Wideband data base from Ancon and Kwajalein to determine the functional forms of the factors, f_r, f_s, f_t, f_λ, as described below. First, we converted the Wideband σ_ϕ^2 values to C_sL values. This was possible since σ_ϕ^2 can be expressed as the product of C_sL and various factors depending only on geometry and on the previously determined parameters. (See Sections 2.2 and 3.) From this point, our plan of action was as follows:

(1) find f_r by examining the dependence of $\sqrt{C_sL}$ on $\bar{R}$.

(2) find f_s by examining the dependence of $\sqrt{C_sL}/f_r(\bar{R})$ on τ.

(3) find f_t by examining the dependence of $\sqrt{C_sL}/[f_r(\bar{R})f_s(\tau)]$ on t_e

(4) find f_λ by examining the dependence of $\sqrt{C_sL}/[f_r(\bar{R})f_s(\tau)f_t(t_e)]$ on λ_a.

These steps were taken in the order of decreasing data-base complication, as observed in exploratory analysis. The objective was to deal with the complications as early as possible, to minimize contamination of later steps.

In each step, the function sought was expressed in terms of two or three constants, which were to be evaluated by choosing them to minimize the mean square error between corresponding function values and data values. The separable-function approach is justified only if the variables R, τ, t_e, and λ_a are uncorrelated or, at most, weakly correlated. Weak correlation turned out to be approximately true; some qualifications are noted below in the discussion of results. The successive normalizations were done to minimize whatever correlation effects there may be. The final step in our procedure was to find C_E as

$$C_E = \sqrt{C_sL} / [\overline{f_r f_s f_t f_\lambda}], \qquad (20)$$

where the bar indicates the function average over the entire Ancon/Kwajalein data base. We shall see that $\overline{f_r f_s f_t f_\lambda}$ turned out to be nearly equal to $\bar{f}_r \bar{f}_s \bar{f}_t \bar{f}_\lambda$, which supports our assumption of weak correlation.

4.2 RESULTS

The significant details in our determination of the four functions and the lead constant in the representation for $\sqrt{C_sL}$ will now be described.

4.2.1. Solar-cycle Variation

Scatter plots of log $\sqrt{C_sL}$ vs log $\bar{R}$ for all Wideband equatorial data are shown in Figure 8, Ancon and Kwajalein data being displayed separately. Since solar activity

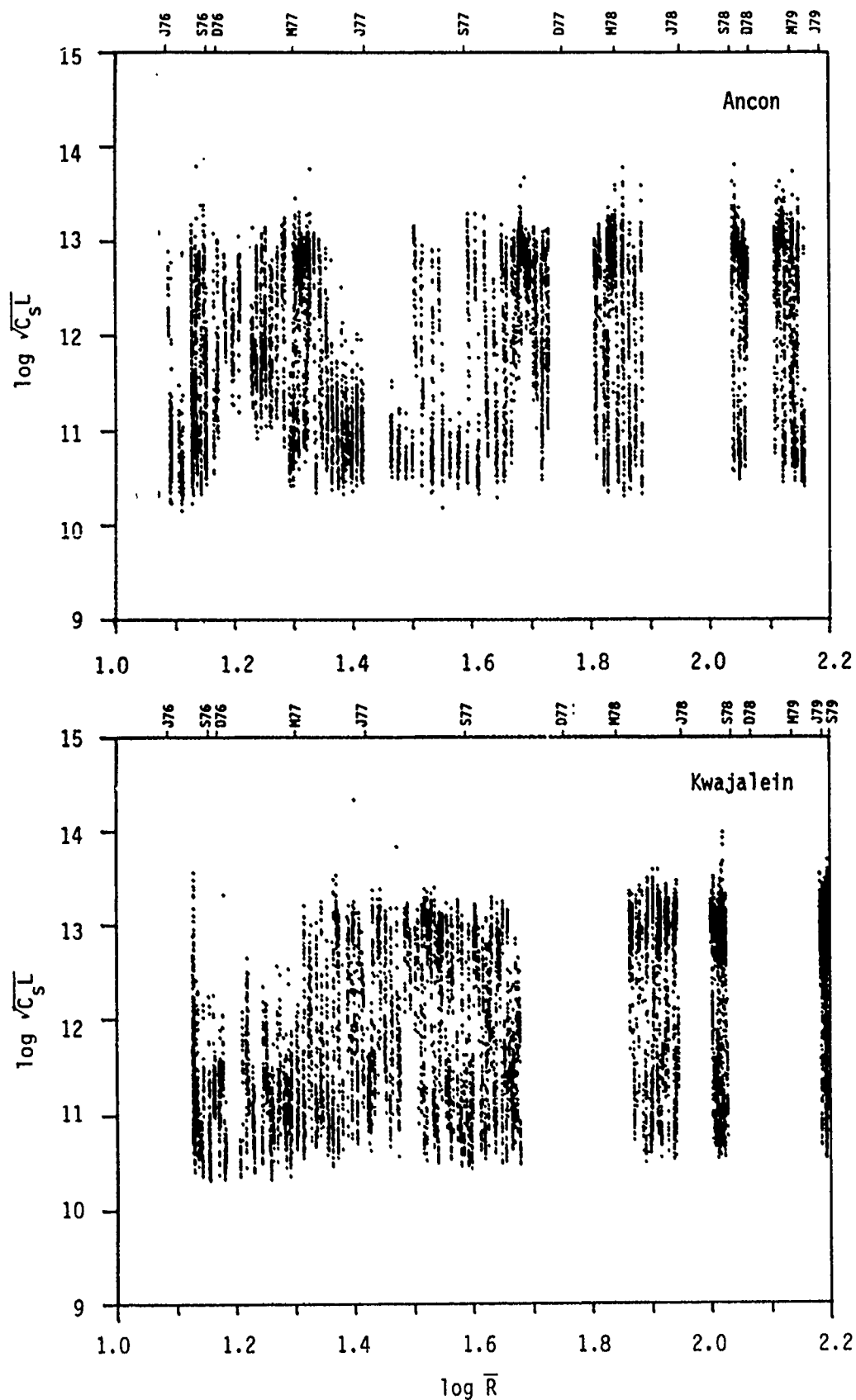33

Figure 8. Scatter plots of log $\sqrt{C_sL}$ vs log $\bar{R}$, where $\bar{R}$ is smoothed sunspot number, for Ancon and Kwajalein. Equinoxes and solstices are indicated at points coincident with the appropriate log $\bar{R}$ value.

varied from minimum to near maximum during the term of the Wideband experiment, the log $\bar{R}$ coordinate in Figure 8 is a measure of advancing epoch. Equinoxes and solstices that occurred during the Wideband Mission are indicated at the top of the plot in Figure 8, located coincidentally with the representative log $\bar{R}$ values for the months of their occurrence.

We can see from Figure 8 that $\sqrt{C_s L}$ generally increases with $\bar{R}$, but that there are broad variations imposed on the increase. These variations are largely seasonal, as can be seen by comparing the peaks and valleys with the equinox and solstice indicators. For $\bar{R} < 60$ (log $\bar{R} < 1.8$), Ancon $\sqrt{C_s L}$ peaks occur approximately at the December solstice and valleys at the June solstice. The behavior is reversed for Kwajalein.

For $\bar{R} > 60$ (log $\bar{R} > 1.8$), we find substantial gaps in the data, with points generally occurring only during peak seasons. These gaps result from the data collection strategy employed in the latter half of the Wideband Mission, which was to observe only during those seasons when scintillation was perceived to be most likely. Since the seasonal variable in our representation for $\sqrt{C_s L}$ is not day-of-year, but τ, it is useful to look at a scatter plot of τ vs log $\bar{R}$, which is shown in Figure 9. We see that the data collection periods for $\bar{R} > 60$ (log $\bar{R} > 1.8$) correspond predominantly to $\tau < 0$ at Ancon and $\tau > 0$ at Kwajalein. Thus, there is a built-in correspondence between these τ regimes and the epoch of increased scintillation.

We see from Figure 10, which shows a scatter plot of log $\sqrt{C_s L}$ $vs \tau$, that $\sqrt{C_s L}$ peaks at Ancon for $\tau < 0$ and at Kwajalein for $\tau > 0$. This behavior is not consistent with the Tsunoda-Wittwer postulate, which calls for a peaking of $\sqrt{C_s L}$ at $\tau = 0$. We expected that by finding $f_r(\bar{R})$ and dividing the $\sqrt{C_s L}$ data by it, we would produce a $\sqrt{C_s L}/f_r(\bar{R})$ data set that would peak at $\tau = 0$. This expectation was based on the notion that the observed peaking at $\tau \neq 0$ was caused by the correspondence of values of $\bar{R} > 60$ to $\tau < 0$ at Ancon and to $\tau > 0$ at Kwajalein.

In order to obtain $f_r(\bar{R})$, we first restricted the data set to those Ancon points for which $\tau < 0$ and those Kwajalein points for which $\tau > 0$. This selection was made to avoid the influence of seasonal minimum data, which were collected only when $\bar{R} < 60$. The resulting data set showed an approximately linear dependence between $C_s L$ and $\bar{R}$, so a least-squares fit to a function of the form $A\sqrt{1+C_r R}$ was performed to obtain $f_r(\bar{R})$. The result was $A = 1.3$ E12 and $C_r = 0.18$; A was absorbed into the lead constant. Figure 11 shows a plot of $Af_r(\bar{R})$ superimposed on bin-averaged points from the τ-restricted data set. Circles indicate Ancon data, and X's indicate Kwajalein data; the width of
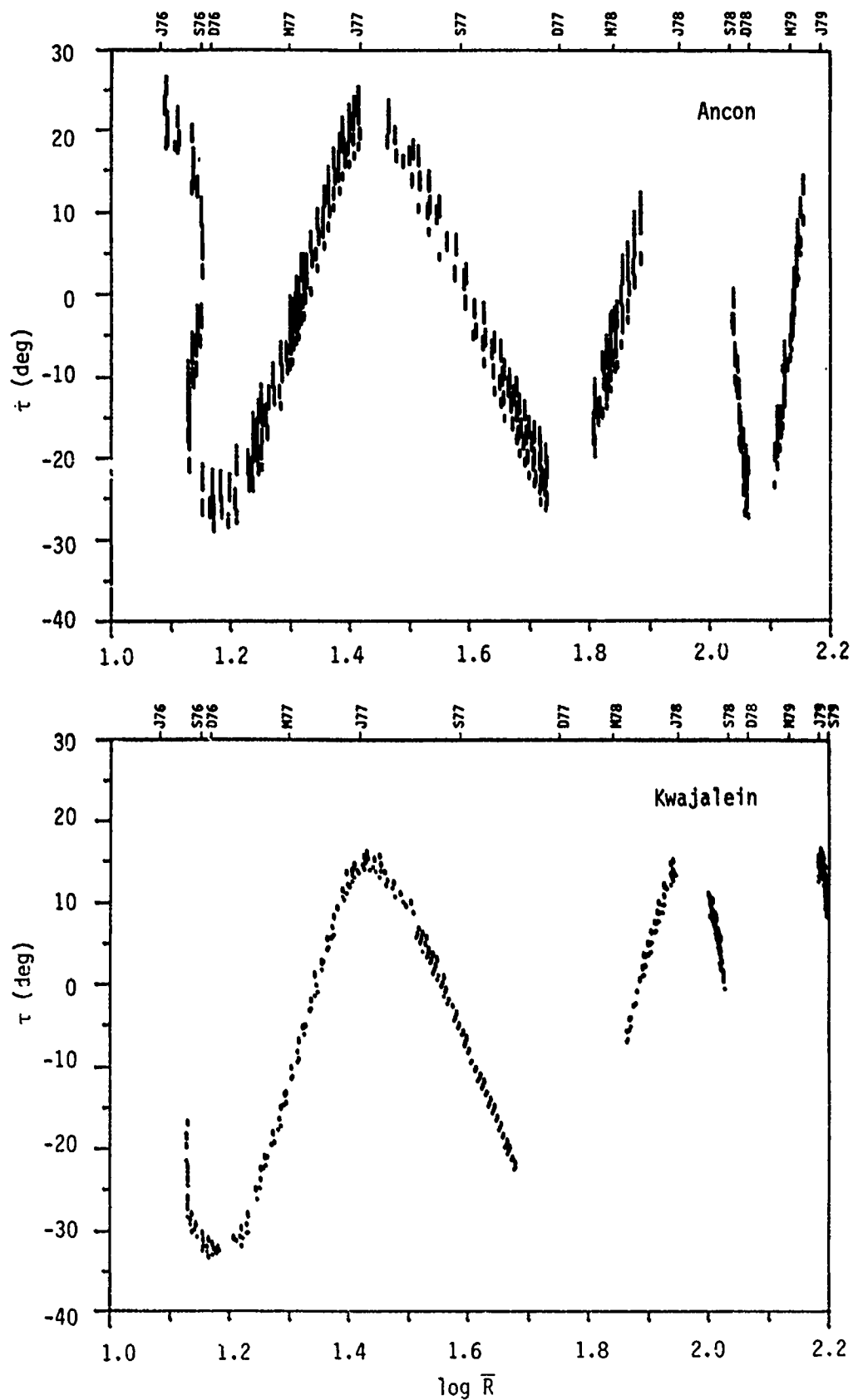
Figure 9. Scatter plots of the magnetic heading of the solar terminator, τ, vs log R̄, where R̄ is smoothed sunspot number, for Ancon and Kwajalein. Equinoxes and solstices are indicated at points coincident with the appropriate log R̄ values.
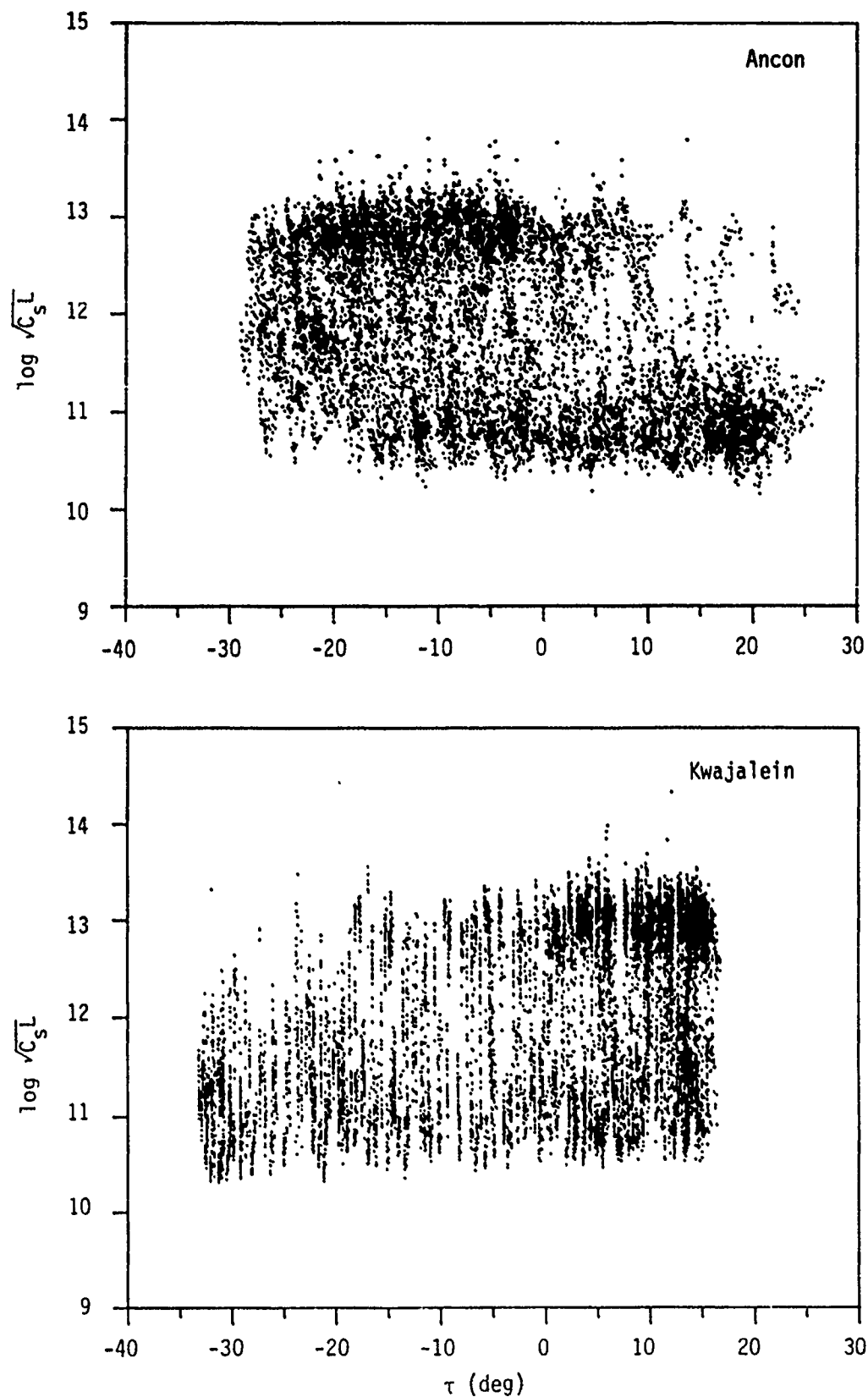
Figure 10. Scatter plots of log $\sqrt{C_s L}$ vs magnetic heading of the terminator for Ancon and Kwajalein.
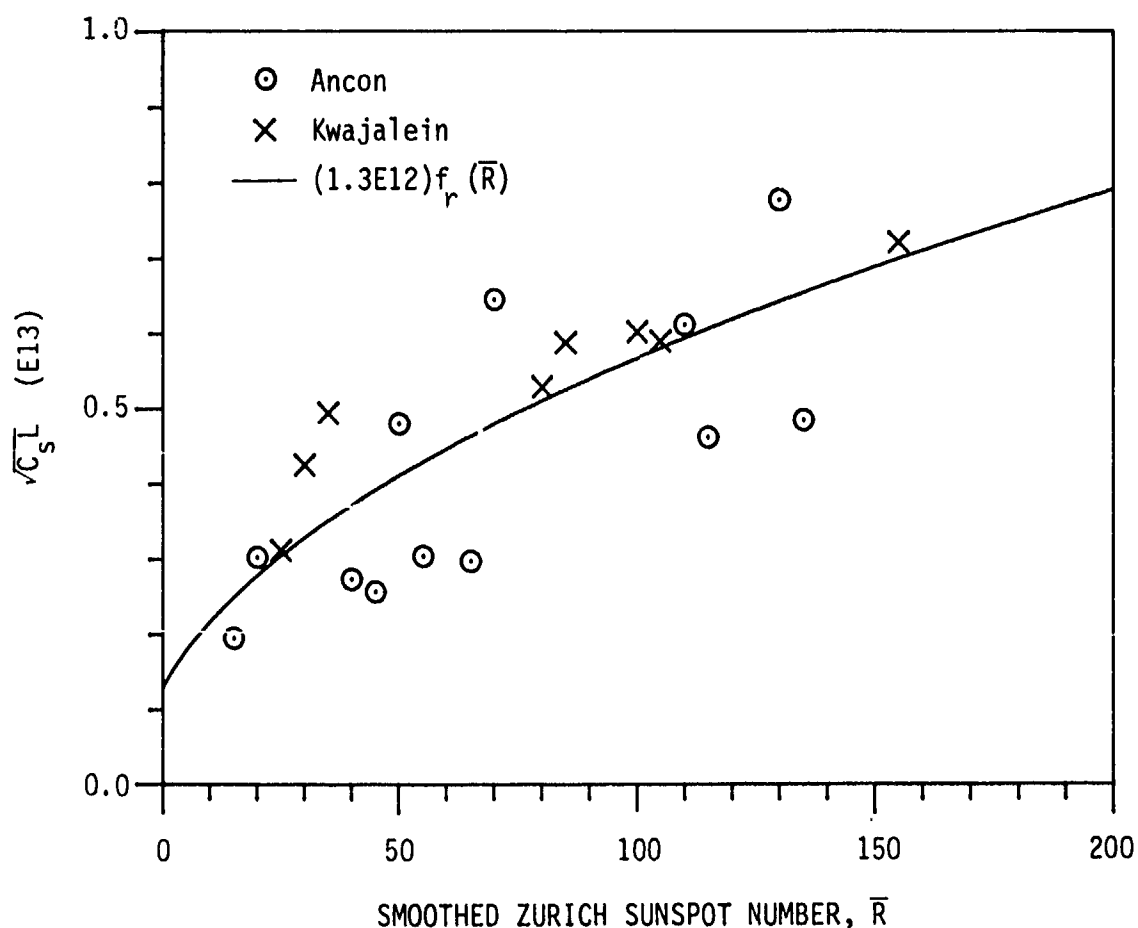
Figure 11. Plot of $(1.3E12)f_r(\overline{R})$ superimposed on bin-averaged $\sqrt{C_sL}$ data from Ancon (◉) and Kwajalein (✕). $\overline{R}$ bins are 5 units wide, and only bins with 200 or more points are shown.

the R-bins was 5 units. Bins containing fewer than 200 points are not shown. Further discussion of the τ-dependence appears below.

4.2.2 Seasonal/longitudinal Dependence

Figure 12 shows scatter plots of $\sqrt{C_sL}/f_r(\overline{R})$ vs τ for the entire Ancon and Kwajalein data sets. It can be seen that consistency with the Tsunoda-Wittwer postulate still is lacking; the data continue to show a shift in peak $\sqrt{C_sL}$ away from $\tau=0$, toward the local summer season. Thus, it appears that some factor besides the longitudinal conductivity gradient invoked by the postulate contributes to control of the seasonal variation of post-sunset ionospheric irregularity strength.

There are several effects that plausibly could compete with the Tsunoda-Wittwer mechanism for seasonal control. Consistent with the observed preference for scintillation to occur during local summer is the notion that enhanced residual post-

Figure 12. Scatter plots of $\log(\sqrt{C_sL}/f_r(\overline{R}))$ vs magnetic heading of the terminator for Ancon and Kwajalein.

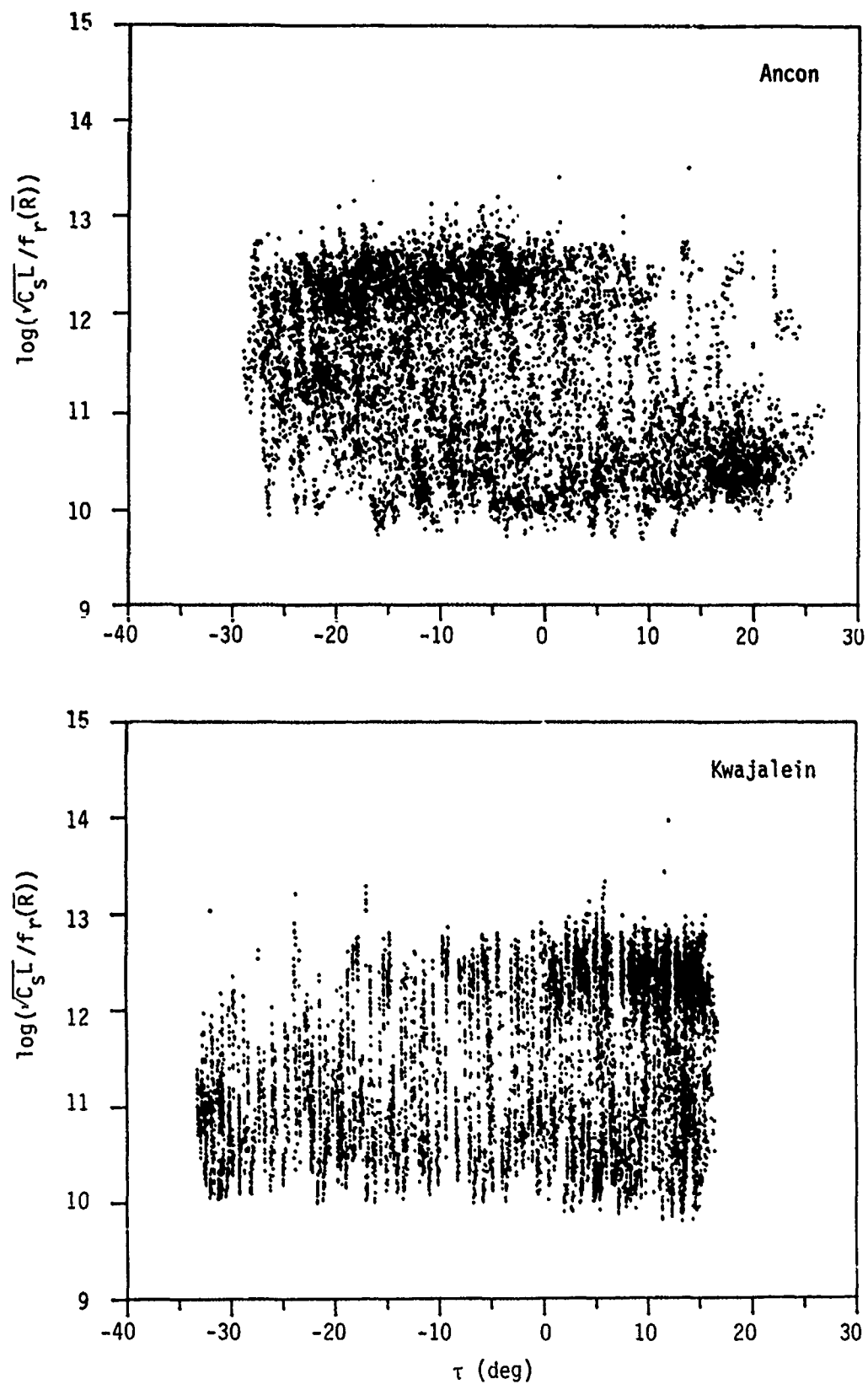sunset TEC in the summer hemisphere may simply produce stronger scintillations for a given percent irregularity strength. Although diffusion would be expected to equalize the residue fairly rapidly along a given flux tube, we did parameterize asymmetric residue in terms of hours of sunlight per day at the F-layer penetration point. The effort was somewhat successful in reproducing the observations, but the result was far from satisfactory.

Likelier candidates involve interaction of thermospheric winds with the plasmasphere. An empirical temptation arose to parameterize the seasonality of equatorial scintillation on the basis of *in-situ* measurements of plasma depletion by Dachev and Walker (1982). From several years of Atmospheric Explorer data, they found clear asymmetry in F-layer plasma density about the magnetic equator during solstice periods and symmetry near the equinoxes. Specifically, they found appreciably lower densities on the summer side of the magnetic equator, inferring that meridional winds blowing from the summer to winter hemisphere had raised the F layer above the satellite altitude on the summer end of flux tubes.

Since a high F layer is favorable to Rayleigh-Taylor instability, one is tempted to make a direct link between Dachev and Walker's result and Wideband's preference for summertime equatorial scintillation. The link would be a weak one, however, in view of the near-perfect electrostatic coupling that exists along geomagnetic flux tubes.

Theoretically, a stronger link could be forged on the basis of work by Maruyama and Matuura (1984). They found clear evidence that F-layer bubbles and topside equatorial spread F preferentially occur at longitudes and in seasons that produce symmetry in plasma density across the magnetic equator. These combinations of longitude and season are largely consistent with the results of Dachev and Walker and can be understood by including the plasmaspheric effects of zonal as well as meridional neutral winds.

An important element of the geometry is orientation of the flux tubes relative to the vector wind, one consequence being that regions of large magnetic declination, such as the Atlantic sector, should be particularly susceptible to Rayleigh-Taylor instability. Moreover, the opposite signs of the declination there and in the Pacific ˉector produce different seasonal variations.

We attempted to parameterize the longitudinal/seasonal variation of scintillation in terms of a combination of the solar-terminator (Tsunoda-Wittwer) and neutral-

wind (Maruyama-Matuura) effects and were able to produce reasonable agreement with the Wideband data base from Kwajalein. We were not able, however, to produce a simultaneously good fit for Ancon.

Finding no factor to shift the modeled C_sL peak from $\tau = 0$ toward the broad summertime peak observed at the two stations, we were forced to leave the unknown factor as a subject for future research and to represent $f_s(\tau)$ simply as $\exp[-(\tau/w_\tau)^2]$. Using the combined Ancon and Kwajalein $\sqrt{C_sL}/f_r(\bar{R})$ data set, we performed a least-squares fit to B times the above qaussian function, with the result that $B = 1.3E12$ and $w_\tau = 27°$; B was absorbed into the lead constant. Figure 13 shows a plot of $Bf_s(\tau)$ superimposed on bin-averaged points from the $\sqrt{C_sL}/f_r(\bar{R})$ data set. Circles denote Ancon data, and X's denote Kwajalein data. The width of the τ-bins was $2°$, and bins containing fewer than 200 points are not shown.
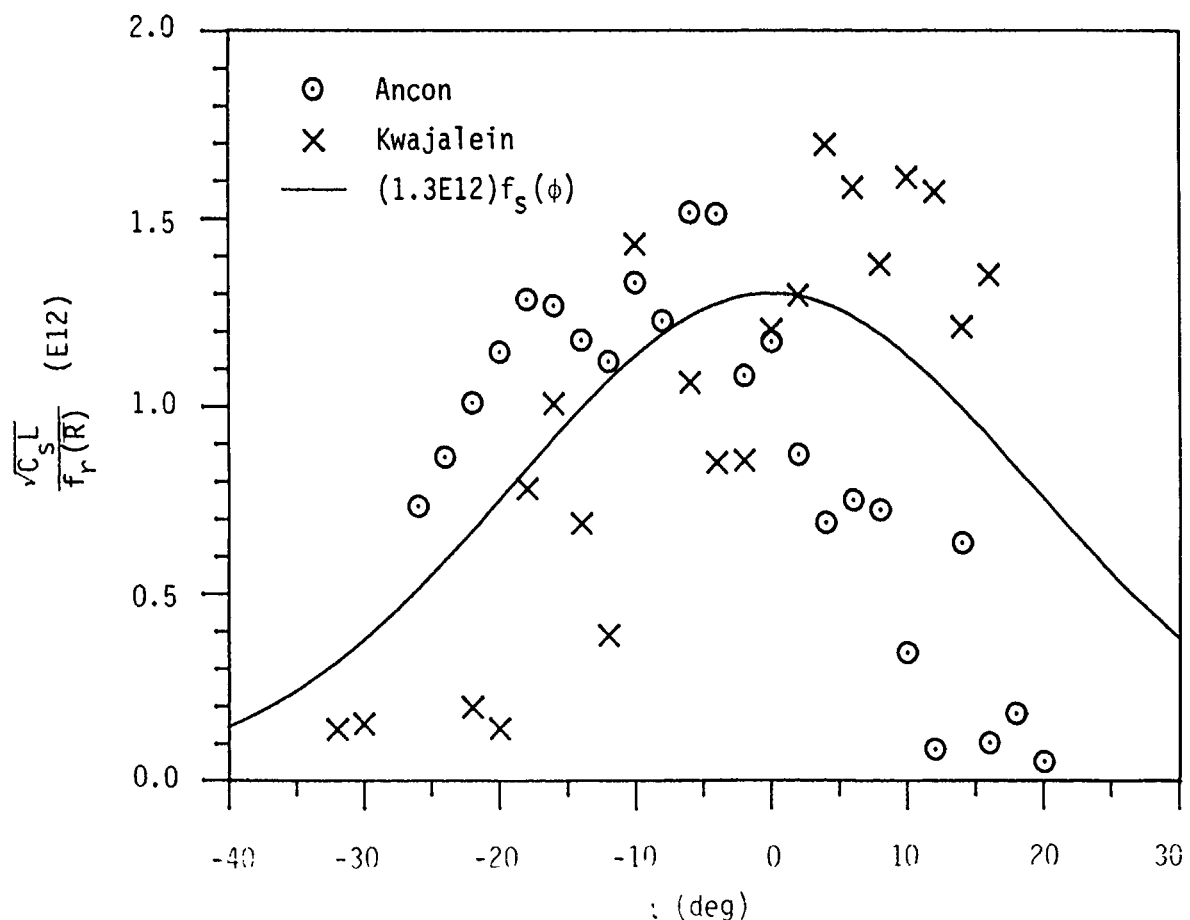

Figure 13. Plot of $(1.3E12)f_s(\tau)$ superimposed on bin-averaged $\sqrt{C_sL}/f_r(\bar{R})$data from Ancon (⊙) and Kwajalein (X). R bins are 5 units wide, and only bins with 200 or more points are shown.

41

4.2.3 Diurnal Variation

Figure 14 shows scatter plots of $\sqrt{C_s L}/[f_r(\bar{R})f_s(\tau)]$ vs t_e for Ancon and Kwajalein. The interval containing data from either station is approximately $t_e = 3.0$ to 5.25 hours. We decided that this t_e interval was too small to justify using only Wideband data to define a function over the range of t_e for which scintillation is expected to occur, namely from 0 to about 12 hours. Instead, we based our choice of $f_t(t_e)$ on the data presented by Aarons et al (1980), which show percentage of scintillation occurence vs local time at four stations: Accra, Ghana; Natal, Brazil; Huancayo, Peru; and Guam. The data shown are for quiet and disturbed magnetic conditons and for various seasons between June 1977 and June, 1979. In general, the data show a relatively sharp increase in scintillation activity, starting at sunset, to a pre-midnight peak, followed by a gradual decrease in activity to quiet conditions at sunrise. In some cases, there is a secondary peak between midnight and sunrise.

To choose $f_t(t_e)$, we assumed that this general pattern would occur as a function of t_e as well as of local time. We ignored the secondary peak after midnight, leaving it as a subject for future research. We were guided by the Ancon data in Figure 14 to describe the $\sqrt{C_s L}$ peak as rather flat, and by visual estimates from Figure 14 to center the peak at $t_e = 4$ hours. Putting all this together, we arrived at the following form for $f_t(t_e)$:

$$
f_t(t_e) = \begin{cases}
\exp\left[-\left(\dfrac{t_e - 3.5}{1.5}\right)^2\right] & t_e \le 3.5 \qquad\qquad (21a)\\[2ex]
1 & 3.5 < t_e < 4.5 \qquad (21b)\\[2ex]
\exp\left[-\left(\dfrac{t_e - 4.5}{4.0}\right)^2\right] & 4.5 \le t_e \qquad\qquad (21c)
\end{cases}
$$

4.2.4 Latitude Dependence

In the previous version of WBMOD, the magnetic latitude dependence of equatorial $\sqrt{C_s L}$ was represented by a function that increases toward the north and south from a non-zero value at the magnetic equator and which peaks on its way to an asymptote of zero at mid-latitudes. This representation was motivated by an observed increase in preliminary Wideband σ_ϕ data as a function of absolute magnetic latitude, and the knowledge that scintillation is relatively weak at mid-latitudes.
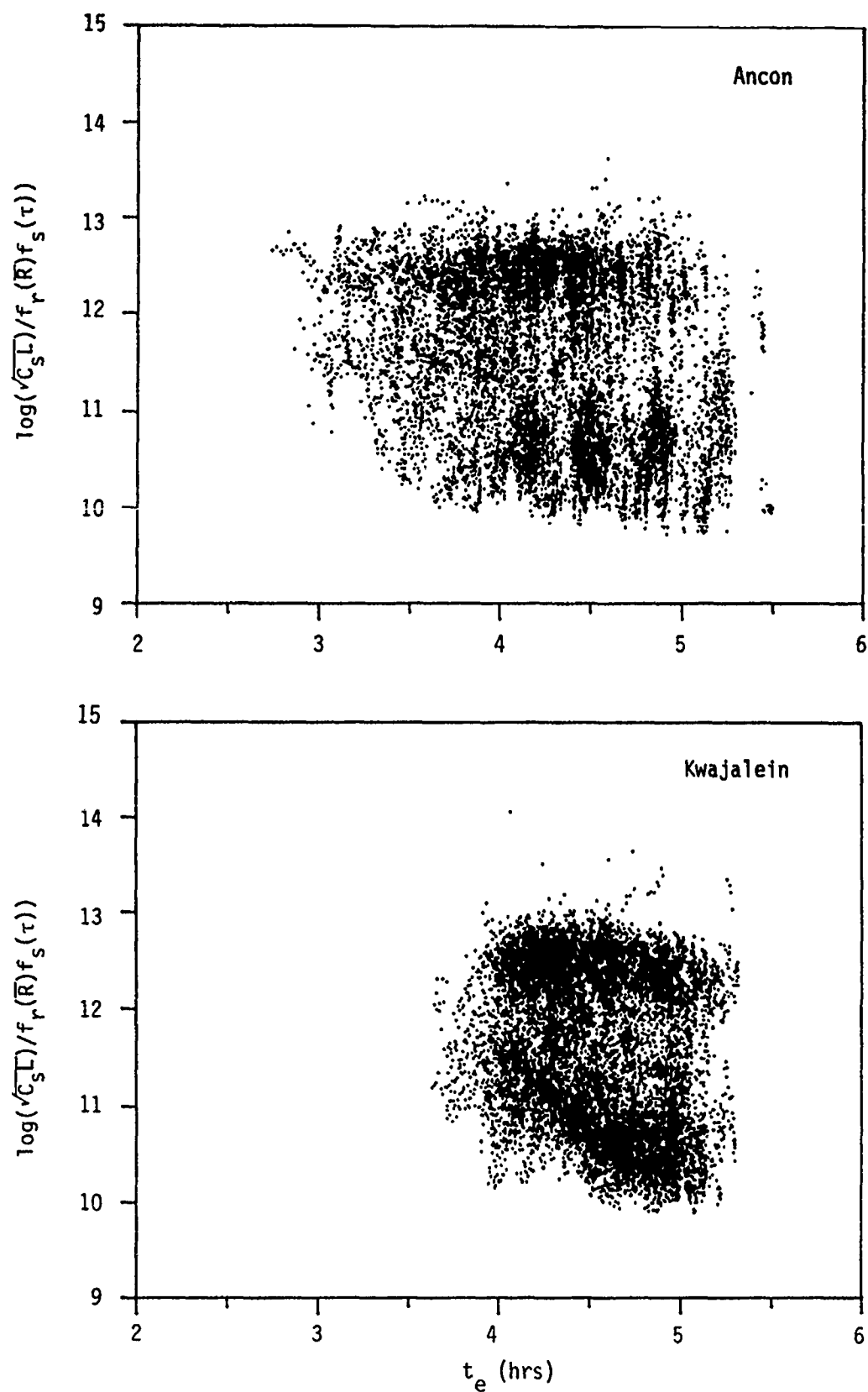
Figure 14. Scatter plots of log $(\sqrt{C_s L}/f_r(\bar{R})f_s(\tau))$ vs t_e, the time after E-layer sunset, for Ancon and Kwajalein.

Figure 15 shows scatter plots of $\sqrt{C_s L} / [f_r(\bar{R}) f_s(\tau) f_T(t_e)]$ vs λ_a for Ancon and Kwajalein. Figure 16 shows bin average points from the data in Figure 15. The width of the bins is 1°, and bins containing fewer than 200 points are not shown. We see that $\sqrt{C_s L}$ increases toward the south at Ancon and shows a slightly increasing trend toward the north at Kwajalein. The previously observed increase in σ_ϕ as a function of $\underline{absolute}$ magnetic latitude at each station evidently stemmed from geometrical enhancement. Since the $\sqrt{C_s L}$ vs λ_a behavior is not consistent between Ancon and Kwajalein, we combined the results and represent the equatorial behavior of $f_\lambda(\lambda_a)$ as constant. The individual station behavior shown in Figure 15 probably stems from the missing seasonal factor that produces stronger irregularities in the local summer hemisphere than in the winter hemisphere.

We also note that the latitudinal extent of the $\sqrt{C_s L}$ data is not large enough for us to estimate where and how sharply $\sqrt{C_s L}$ drops off toward its mid-latitude asymptote, so we are forced to other sources of information for the break point and decline rate of $f_\lambda(\lambda_a)$. We estimate that

$$f_\lambda(\lambda_a) = 0.5 \left\{ 1 - \mathrm{erf}\left[\frac{|\lambda_a| - 20°}{3°} \right] \right\} \qquad (22)$$

for λ_a in degrees, where erf denotes the error function, $\mathrm{erf}(x) = (2/\sqrt{\pi}) \int_0^x e^{-t^2} dt$. This choice will be checked against Wideband data from Stanford. A plot of $f_\lambda(\lambda_a)$ vs λ_a is shown in Figure 17.

4.2.5 $C_s L$ Lead Constant

From the representation

$$\sqrt{C_s L} = C_e \, f_r(\bar{R}) f_s(\tau) f_t(t_e) f_\lambda(\lambda_a), \qquad (23)$$

it was straightforward to arrive at a value for C_e. Averaging over the entire Wideband equatorial data base, we computed the following mean values:

$$\overline{\sqrt{C_s L}} = \quad 3.47\mathrm{E}12 \qquad (24a)$$

$$\overline{f_r f_s f_t f_\lambda} = 2.51 \qquad (24b)$$

$$\bar{f}_r = \quad 3.17 \qquad (24c)$$

$$\bar{f}_s = \quad 0.78 \qquad (24d)$$

$$\bar{f}_t = \quad 0.99 \qquad (24e)$$

$$\bar{f}_\lambda = \quad 1.00 \qquad (24f)$$

44
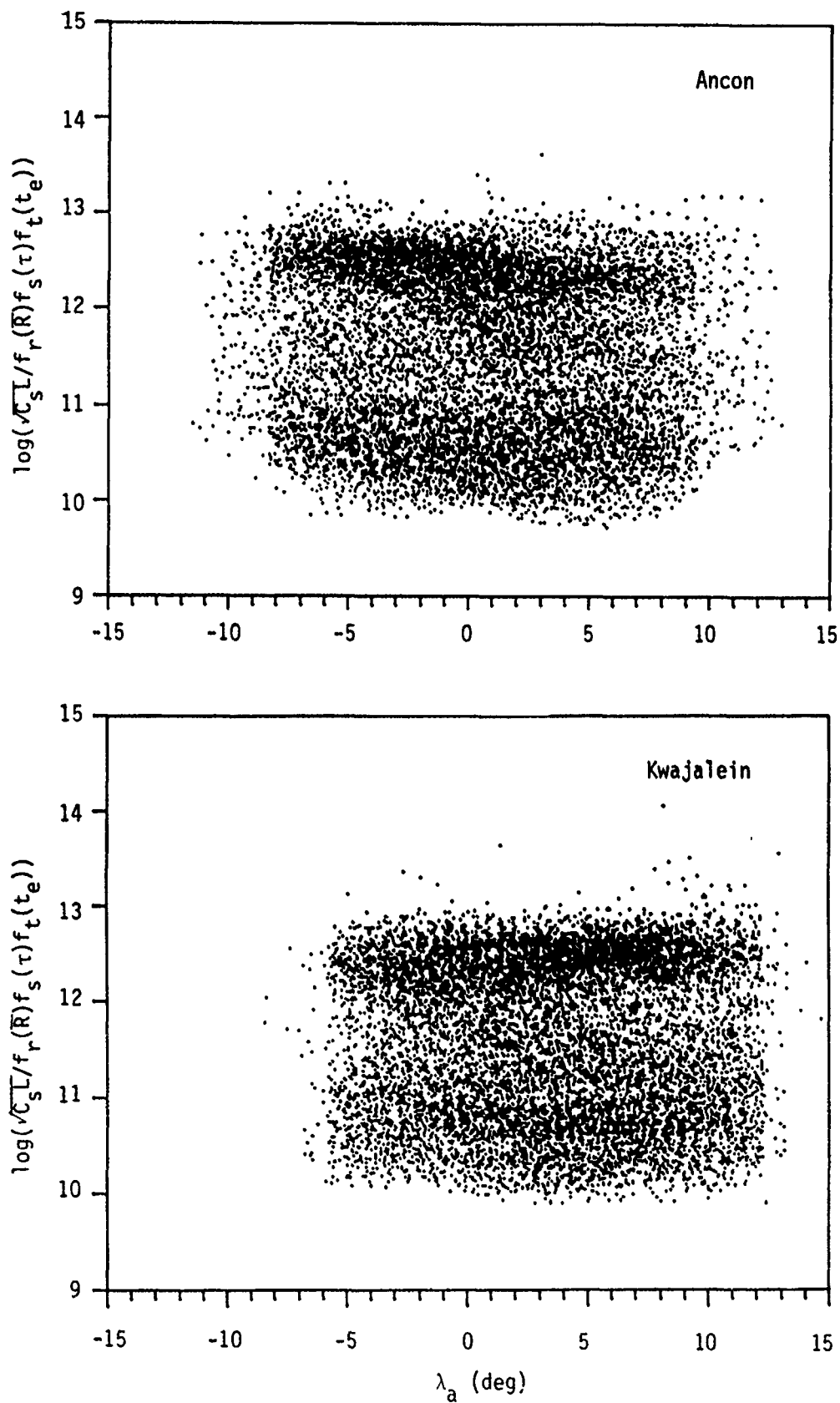
Figure 15. Scatter plots of $\log(\sqrt{C_s}L/f_r(\bar{R})f_s(\tau)f_t(t_e))$ vs F-layer apex latitude, λ_a, for Ancon and Kwajalein. Latitude bins are $1°$ wide, and only bins with 200 or more points are shown.
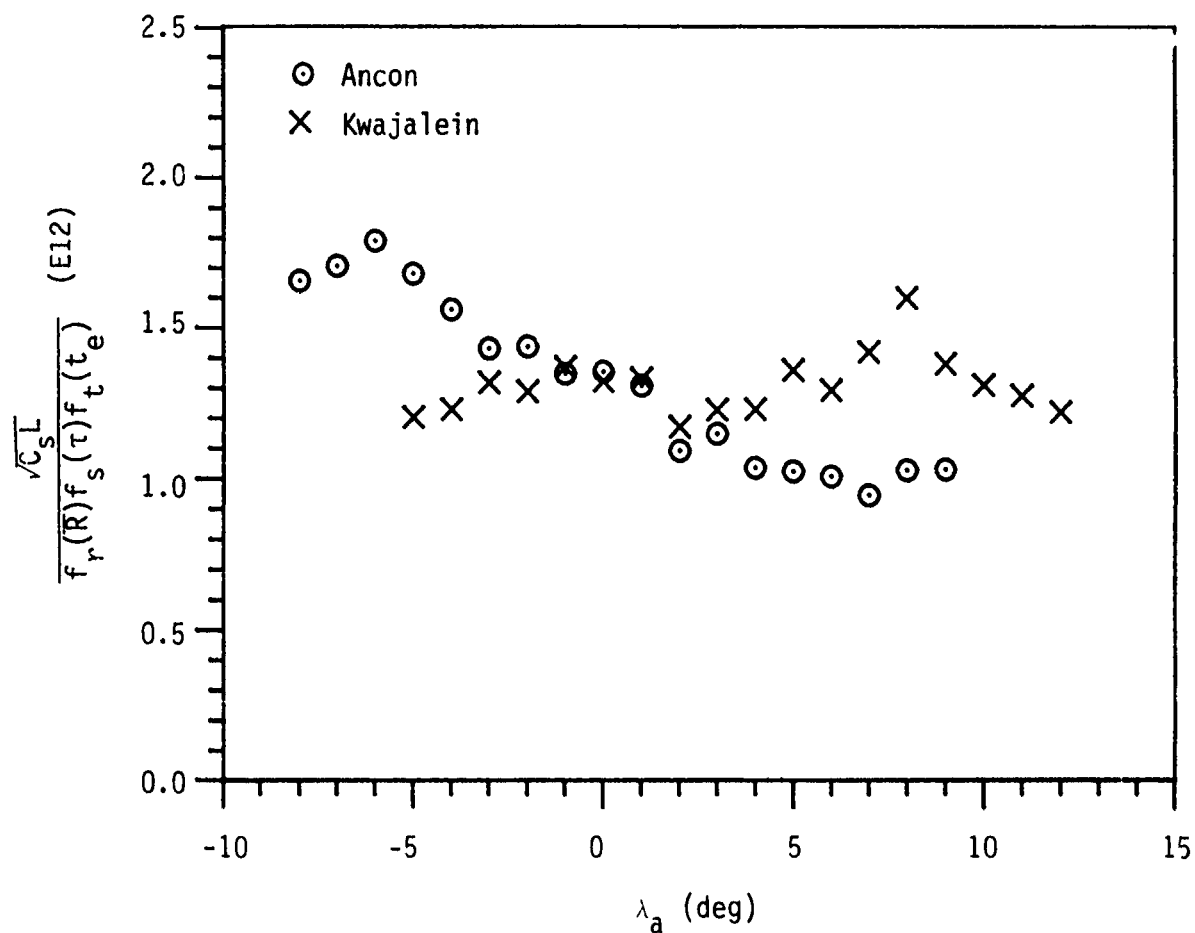
Figure 16. Bin-averaged $\sqrt{C_s L}/f_r(\bar{R})f_s(\tau)f_t(t_e)$ data from Ancon (⊙) and Kwajalein (✕). Latitude bins are 1° wide, and bins containing fewer than 200 points are not shown.
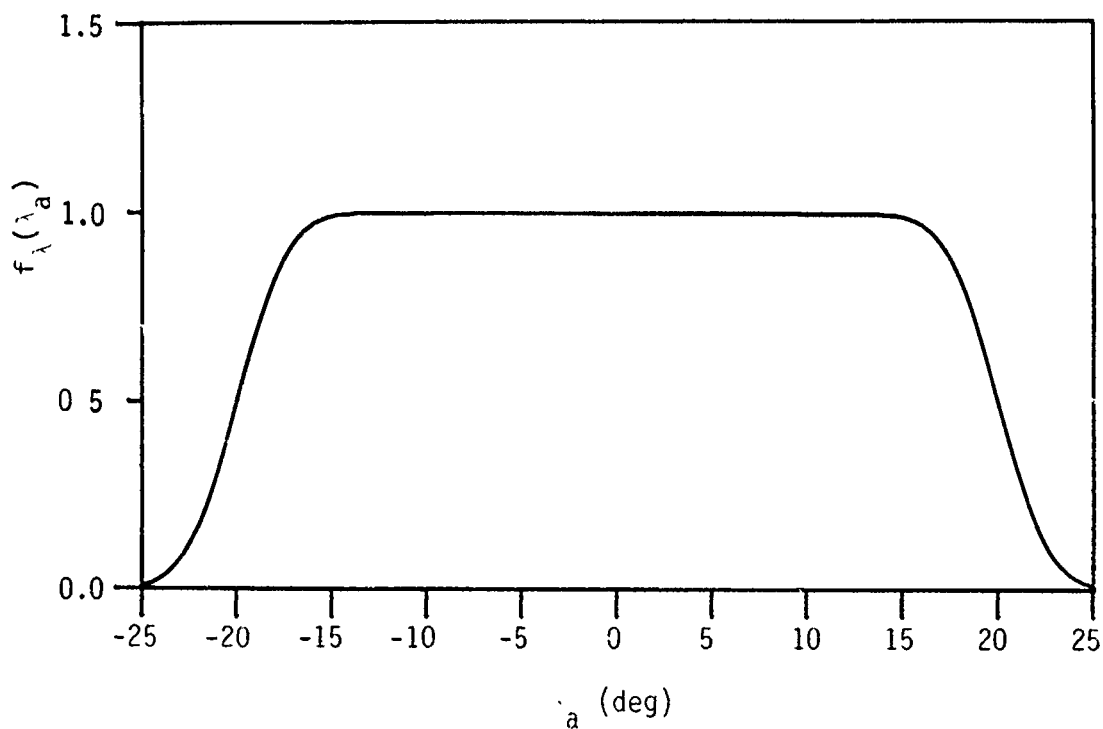
Figure 17. Plot of $f_\lambda(\lambda_a)$ vs the F-layer apex latitude.

46

It follows from Eqs. (24a) and (24b) that

$$C_e = \sqrt{\overline{C_s L}} \, / \, \overline{f_r f_s f_t f_\lambda} = 1.38E12, \tag{25}$$

which we rounded to 1.4E12. We note from Eqs. (24c) through (24f) that $\overline{f_r}\,\overline{f_s}\,\overline{f_t}\,\overline{f_\lambda} = 2.45$, a value quite close to $\overline{f_r f_s f_t f_\lambda}$. This result supports our use of multiplicatively separable factors in Eq. (23).

SECTION 5

EFFICACY AND USE OF WBMOD

5.1 CORRIDOR COMPARISONS

The results from the previous sections were incorporated into WBMOD, and evaluation tests of the new equatorial scintillation model were performed. Statistical evaluations of model outputs and results from model/data comparisons for east, overhead, and west corridors are presented below.

Returning to the three (east, overhead, west) corridor data sets from Kwajalein referred to in Section 3.4, we tested the model by simulating each pass in each of these data corridors. A one-to-one correspondence of model data points to actual data points was obtained. Identical in format to Figure 6, Figure 18 shows plots of the latitudinal variation of mean scintillation strength for the final model and the actual data. Data have been averaged over one-degree latitude bins, and bins with fewer than 50 points are not shown. Model parameters are those presented in Sections 3 and 4. The agreement between model and data can be seen to be reasonably good.

A similar test was performed for Ancon. As for Kwajalein, data corridors to the east, overhead, and west of the receiver were defined. Corridor widths were 3° in longitude. This width was chosen to ensure a statistically significant population in each latitude bin. For Kwajalein, a 2° width was sufficient to accomplish this objective. Numbers of points in each corridor are listed in Table 3.

Table 3. Number of points in data corridors.

	West	Overhead	East
Ancon (3° corridors)	2307	2378	2291
Kwajalein (2° corridors)	1684	2316	2228

As for Kwajalein, model results for the Ancon corridors were obtained in one-to-one correspondence with the observed data. Model/data comparisons for Ancon are shown in Figure 19, where we see that the model results and data are qualitatively similar. If the results for the three Ancon corridors are averaged together, the result is a more quantitative model/data agreement, as shown in Figure 20. For Kwajalein, the model data agreement is quantitive in each corridor, and thus superior to the model/data agreement for Ancon.

48

Figure 18. Plots of bin-averaged WBMOD σ_ϕ results (-----) and bin-averaged Wideband σ_ϕ data (————) vs F-layer apex latitude, for three corridors above Kwajalein. The bins are 1° wide, and bins containing fewer than 50 points are not shown.

49

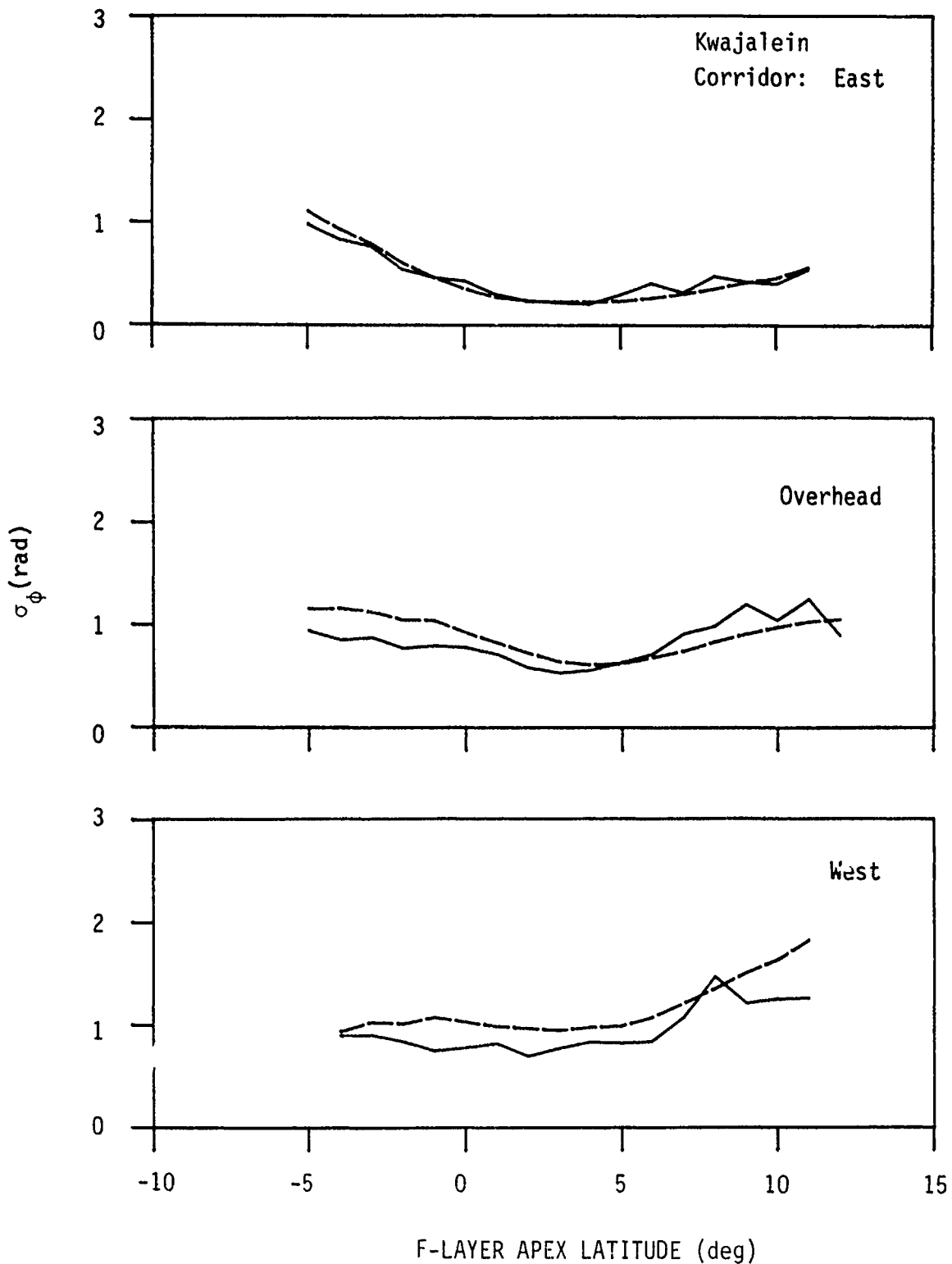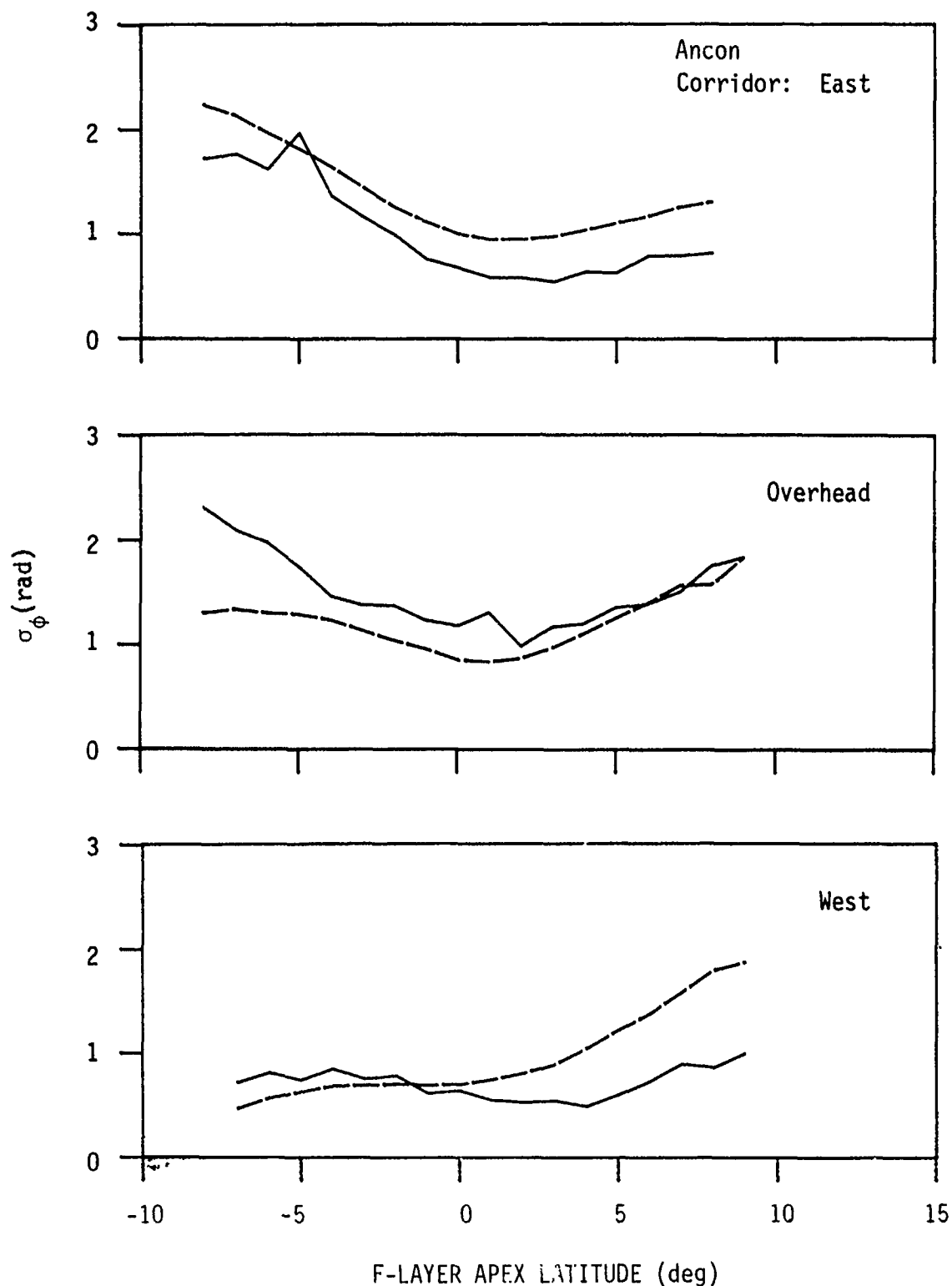Figure 19. Plots of bin-averaged WBMOD σ_ϕ results (-----) and bin-averaged Wideband σ_ϕ data (———) vs F-layer apex latitude, for three corridors above Ancon. The bins are 1° wide, and bins containing fewer than 50 points are not shown.
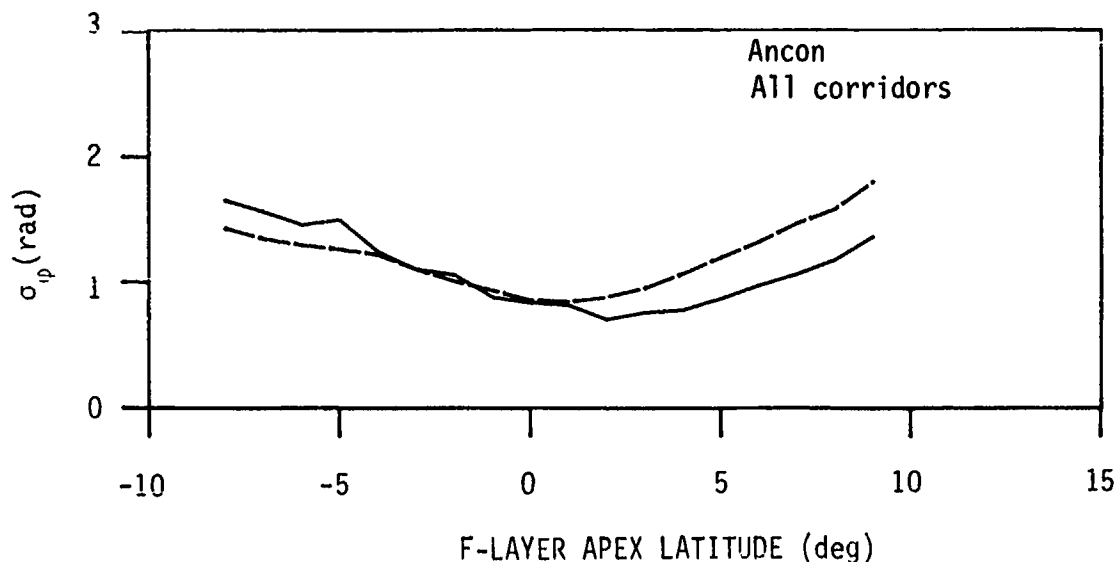
Figure 20. Plot of bin-averaged WBMOD σ_ϕ results (-----) and bin-averaged Wideband σ_ϕ data (———) vs F-layer apex latitude, for a superposition of data from the three Ancon corridors represented in Figure 19. The bins are 1° wide, and bins containing fewer than 150 points are not shown.

Recall that our attempt to use a transequatorial wind model to explain the τ-dependence of the data (Section 4.2.2) also was more successful for Kwajalein than for Ancon. It thus appears that, in some sense, the Kwajalein data are better behaved than the Ancon data. Three conditions potentially responsible for this difference are as follows: (1) the proximity of Ancon to the Andes mountains, a source of internal waves which could serve as a trigger for scintillation events; (2) the strong curvature of the magnetic equator near Ancon; and (3) the greater departure of the magnetic equator from the geographic equator near Ancon. The possible significance of the last two conditions is supported by the comments of Dachev and Walker (1982), who indicate that the geometry of the geomagnetic field seems to play a role in the formation of large-scale equatorial plasma density depletions. The actual importance of the above three conditons remains a subject for future investigation.

5.2 STATISTICAL EVALUATION

Model simulations for each pass in the entire Ancon and Kwajalein data sets were performed, resulting in a one-to-one correspondence between model data ponts and actual data points. Cumulative distribution functions for $(\sigma_\phi)_{data} - (\sigma_\phi)_{model}$, for Ancon and for Kwajalein, then were obtained; they are plotted in Figure 21. The main result to be gleaned from these plots is that the WBMOD equatorial model appears to predict about the 70th percentile of the observed data. That is, about 30% of the time the model underestimates the observed σ_ϕ, and about 70% of the time the model over-estimates it.
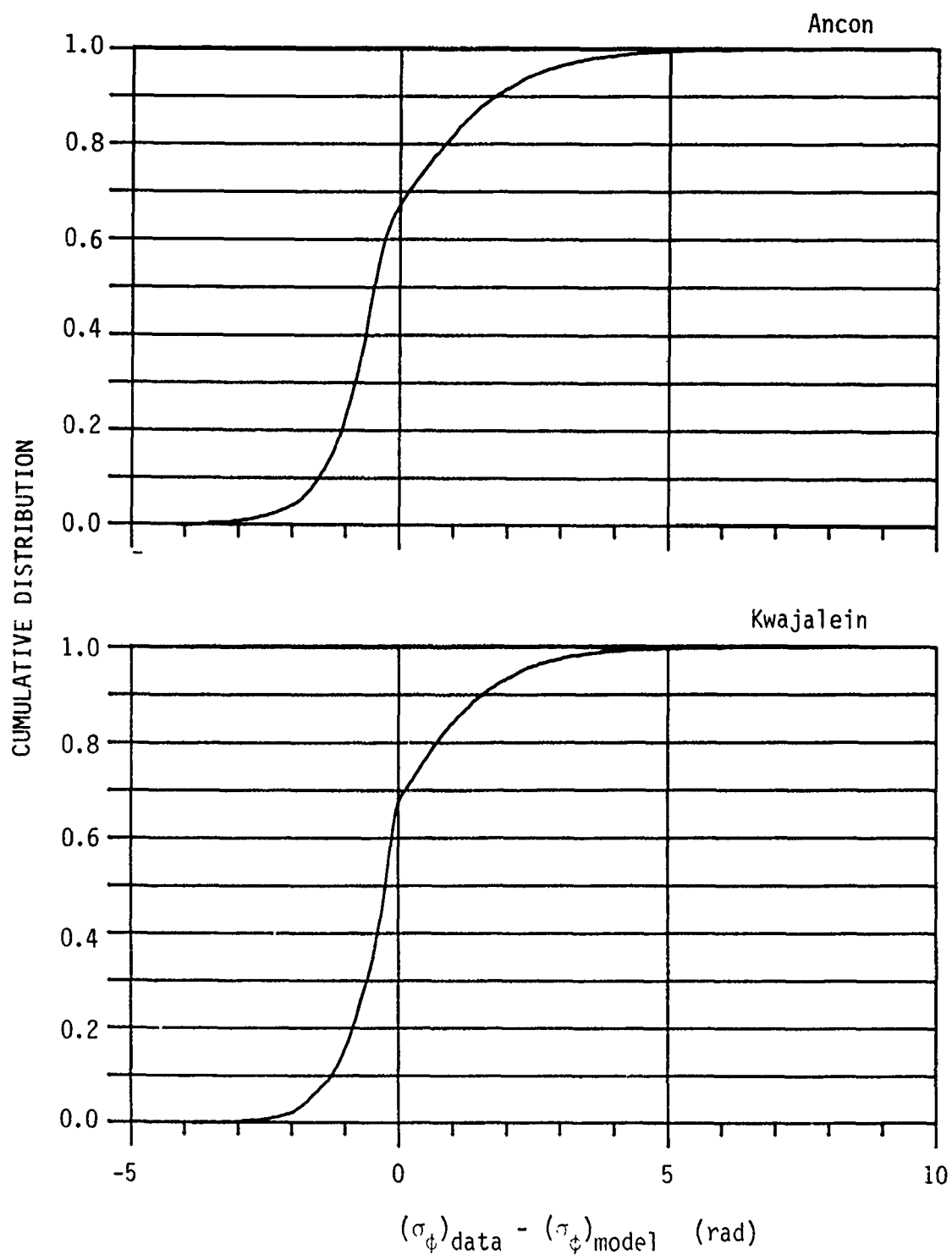
Figure 21. Cumulative distribution functions for the quantity $(\sigma_\phi)_{data}$ - $(\sigma_\phi)_{model}$, where WBMOD model values are in one-to-one correspondence with Wideband data points, for Ancon and Kwajalein.

5.3 REPRESENTATIVE AND QUASI WORST-CASE PREDICTIONS

We have just seen that WBMOD produces σ_ϕ estimates that approximate the 70th percentile of the distribution of equatorial observations. Inasmuch as many nights are devoid of scintillation, this value may be regarded as representative of nights on which scintillation does occur. For some applications, a quasi worst-case estimate may be of interest, and WBMOD now contains such a capability for equatorial applications. The output of a "worst-case" run provides a value of σ_ϕ, say $(\sigma_\phi)_{90}$, that is an estimate of the 90th percentile of observed values.

One could base a "worst-case" capability on the cumulative distribution of $(\sigma_\phi)_{data} - (\sigma_\phi)_{model}$, presumably for Ancon and Kwajalein combined. A plot of that distribution would be like the ones shown in Figure 21, for the individual stations. Moving along such a plot from the ordinate $(\sigma_\phi)_{data} - (\sigma_\phi)_{model} = 0$ to the ordinate 0.9 would correspond to an abscissa increment, $\Delta\sigma_\phi$, that could be used to define $(\sigma_\phi)_{90}$ as $(\sigma_\phi)_{model} + \Delta\sigma_\phi$. A disadvantage of doing so, however, is that it would ignore the possibility that $\Delta\sigma_\phi$ may itself depend on $(\sigma_\phi)_{model}$.

To explore the latter possibility, we returned to the $\sqrt{C_s L}$ data base and plotted cumulative distributions of $(\sqrt{C_s L})_{data} - (\sqrt{C_s L})_{model}$ for low, medium, and high ranges of $(\sqrt{C_s L})_{model}$. These ranges were $\sqrt{C_s L} < .3E13$, $.3E13 < \sqrt{C_s L} < .5E13$, and $.5E13 < \sqrt{C_s L}$, respectively. Results for combined Ancon and Kwajalein data are shown in Figure 22. For each plot in Figure 22, we found the abscissa displacement, $\Delta\sqrt{C_s L}$, required to move along the cumulative distribution curve from $(\sqrt{C_s L})_{data} - (\sqrt{C_s L})_{model} = 0$ to the abscissa for which the ordinate was 0.9. The results are summarized in Table 4, where the values .2E13, .4E13, and .6E13 are taken to be representative of the three $(\sqrt{C_s L})_{model}$ ranges.

Table 4. Adjustments of model to quasi worst case.

value of $(\sqrt{C_s L})_{model}$	$\Delta\sqrt{C_s L}$
.2E13	.39 E13
.4E13	.65 E13
.6E13	.88 E13

In each case, when $(\sqrt{C_s L})_{model}$ is incremented by $\Delta\sqrt{C_s L}$, the result is exceeded by the corresponding data value only 10% of the time. The relationship between the tabulated quantities is nearly linear and can be expressed as
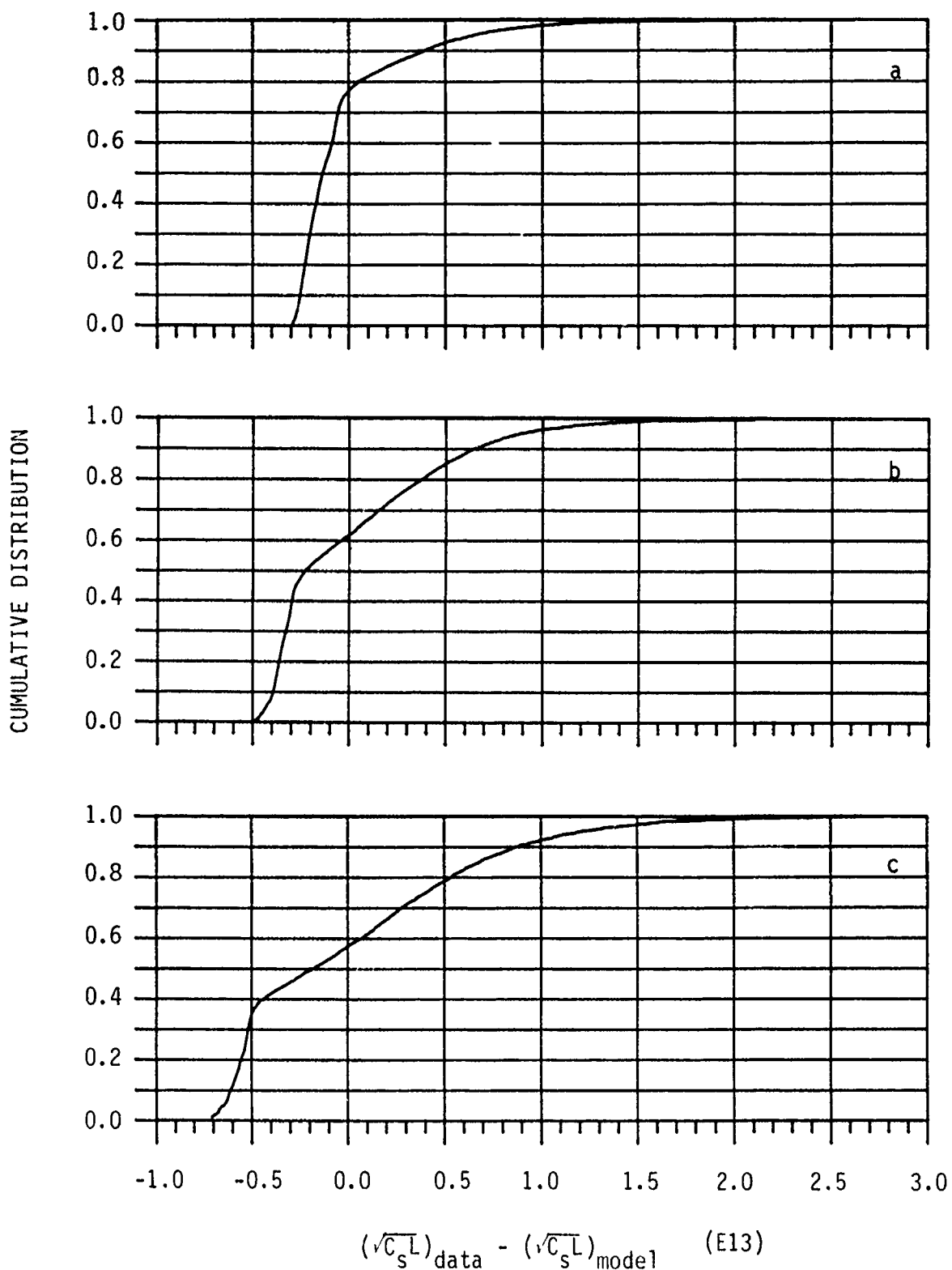
Figure 22. Cumulative distribution functions for the quantity $(\sqrt{C_sL})_{data}$ - $(\sqrt{C_sL})_{model}$, for Ancon and Kwajalein data combined. The WBMOD model values are in one-to-one correspondence with the Wideband data points. Plots (a), (b), and (c) are for the $(\sqrt{C_sL})_{model}$ ranges $\sqrt{C_sL} < 0.3E13$, $0.3E13 < \sqrt{C_sL} < 0.5E13$, and $0.5E13 < \sqrt{C_sL}$, respectively.

$$\Delta \sqrt{C_s L} = 1.25 (\sqrt{C_s L})_{model} + 0.15 \ E13 \tag{26}$$

An option has been added to WBMOD that allows the user to obtain values of T, σ_ϕ, and S_4 corresponding to $(\sqrt{C_s L})_{model} + \Delta \sqrt{C_s L}$. These outputs may be regarded as quasi worst-case values.

SECTION 6

CONCLUSION

This work concludes use of Wideband data for scintillation modeling, except for future combination of the small collection from Stanford, with data from DNA's HiLat (and possibly Polar Bear) satellite(s) in a modest effort to describe mid-latitude scintillation. In several respects, introduced in Section 1 and elucidated in the body of this report, the Wideband data from Ancon and Kwajalein were more limited in their utility for equatorial modeling than were those from Poker Flat for auroral-zone modeling. Nonetheless, the high quality of the Wideband data base has permitted a truly quantitative characterization of scintillation-producing irregularities near the magnetic equator.

As indicated in Table 2, that characterization includes cross-field isotropy, elongation along the magnetic field by a factor of 50, a single-regime power-law spectrum with an *in-situ* spectral index of 1.5, and representation by a phase-modulating screen located at an F-layer altitude of 350 km. In accord with incoherent-scatter observations, the irregularities are taken to drift eastward at night at speeds up to 100 m/s and westward in the daytime at speeds up to half that.

The bulk of the model is its description of the height-integrated spectral strength, C_sL, of the irregularities, by means of the following formulation:

$$\sqrt{C_sL} = C_e f_r(\bar{R}) f_s(\tau) f_t(t_e) f_\lambda(\lambda_a) \tag{27}$$

where $\bar{R}$ = smoothed Zurich sunspot number,

   τ = magnetic heading of the solar terminator at the apex of the magnetic field line through the point of interest,

   t_e = hours after the later sunset at the two E-layer feet of the magnetic field line through the point of interest,

and λ_a = F-layer magnetic apex latitude; and

where $f_r = (1 + 0.18 \, \bar{R})^{\frac{1}{2}}$, $\tag{28}$

$f_s = \exp[(-\tau/27^c)^2]$, $\tag{29}$

$$f_t = \begin{cases} \exp[-(t_e - 3.5)^2/1.5^2] & t_e \leq 3.5 \text{ hrs} & \text{(30a)} \\ 1 & 3.5 \leq t_e \leq 4.5 \text{ hrs} & \text{(30b)} \\ \exp[-(t_e - 4.5)^2/4.0^2] & t_e \geq 4.5 \text{ hrs,} & \text{(30c)} \end{cases}$$

$$f_\lambda = 0.5(1 - \text{erf}\, \frac{|\lambda_a| - 20°}{3°}\,), \tag{31}$$

$$\text{and}\quad C_e = 1.4 \times 10^{12}\, \text{el}/\text{m}^2. \tag{32}$$

Direct application of the foregoing model in WBMOD Version 8D1 yields estimates of representative scintillation indices corresponding to the 70th percentile of phase scintillation strength observed at Kwajalein, Marshall Islands, and Ancon, Peru, under conditions prescribed by the independent variables defined in conjunction with Equation (27). A "worst-case" option has been incorporated for equatorial application of WBMOD, which will return estimates corresponding instead to the 90th percentile observed under the same conditions.

The equatorial model in WBMOD does not attempt to describe variations in scintillation activity with geomagnetic conditions, which constitute some of the remaining statistical deviations from the model. Neither does it include the secondary diurnal maximum sometimes observed in the post-midnight hours, which could be added fairly easily in an *ad hoc* fashion but which was not amenable to testing against Wideband data because of the satellite's sunsynchronous orbit. Another characteristic excluded because Wideband data concerning it are not available is the qualitatively known longitudinal maximum in the Atlantic (magnetic-anomaly) sector of the equatorial region. Again, a reasonable estimate of this behavior probably could be introduced in an *ad hoc* way.

The biggest remaining difficulty in reliable modeling and characterization of trends in the occurrence statistics of equatorial scintillation remains that of accurately describing its joint dependence on season and longitude. We have incorporated a description based on the work of Tsunoda (1985) and believe it to be suitable at most locations. We base this belief on Tsunoda's own multi-station analysis and on independent confirmation from the Indian sector (P. Pasricha, private communication). Our Tsunoda-based formulation also characterizes the amalgamated behavior of Wideband data from Ancon and Kwajalein reasonably well. (See Figure 13.) When data from the two stations are separated, however, we see a systematic departure from that behavior. The departure is a skewing of the season of maximum scintillation activity toward the local summer at each station.

From the work of Dachev and Walker (1982) and of Maruyama and Matuura (1984) and from discussions with D. Anderson of the Air Force Geophysics Laboratory, we suspect that a missing factor in the seasonal/longitudinal variation of equatorial scintillation involves thermospheric winds. An effect worth pursuing in depth is the wind's

driving of plasma along field lines into the winter hemisphere. If such plasma reaches sufficiently low altitudes, it would compete with locally produced ionization for control of the field-line integrated Pedersen conductivity, and it also could accelerate damping by recombination. The prediction of Tsunoda and the control of scintillation onset by E-layer sunset then could be disrupted.

The Wideband data from Kwajalein seem consistent with the foregoing suggestion, but we were not able to formulate a description that also satisfied the Ancon data. We note that the situation at Ancon might be particularly complicated since the magnetic declination in its F-layer field of view changes very rapidly with longitude, declination being a key factor both in terminator control of onset and in the seasonal variation of field-aligned neutral-wind strength.

We suggest that more detailed modeling of equatorial neutral winds and their effect on plasma electrodynamics is likely to facilitate completion of equatorial scintillation modeling. Meanwhile, we believe that WBMOD Version 8D1 may be used quite satisfactorily for estimating representative and quasi worst-case levels of equatorial scintillation to be expected at specified times and places on transionospheric radio and radar links operating at VHF and above.

SECTION 7

LIST OF REFERENCES

Aarons, J., J.P. Mullen, J.P. Koster, R.F. daSilva, J.R. Medeiros, R.T. Medeiros, A. Bushby, J. Pantoja, J. Lanat, and M.R. Paulson (1980), "Seasonal and Geomagnetic Control of Equatorial Scintillations in Two Longitudinal Sectors," J. Atmos. Terr. Phys., 42, 861-866.

Basu, Santimay and Sunanda Basu (1981), "Equatorial Scintillations--A Review," J. Atmos. Terr. Phys., 43 (5/6), 473-489.

Basu, Santimay, J. P. McClure, Sunanda Basu, W. T. Hanson, and J. Aarons (1980) "Coordinated Study of Equatorial Scintillation and In Situ and Radar Observations of Nighttime F Region Irregularities," J. Geophys. Res., 85 (A10), pp. 5119-5130.

Briggs, B. H., and I. A. Parkin (1963), "On the Variation of Radio Star and Satellite Scintillations with Zenith Angle," J. Atmos. Terr. Phys., 25 (6), 339-366.

Christiansen, R.M. (1971), "Preliminary Report of S-Band Propagation Disturbance During ALSEP Mission Support (November 19, 1969 - June 30, 1970)," Goddard Space Flight Center, Greenbelt Maryland, Report No. X-861-71-239.

Cronyn, W. M. (1970), "The Analysis of Radio Scattering and Space-Probe Observations of Small-Scale Structure in the Interplanetary Medium," Astrophys. J., 161, 755-762.

Dachev, Ts. P. and J.C.G. Walker (1982), "Seasonal Dependence of the Distribution of Large-Scale Plasma Depletions in the Low-Latitude F Region," J. Geophys. Res., 87 (A9), 7625-7639.

Fejer, B.G., D.T. Farley, C.A. Gonzales, R.F. Woodman, and C. Calderon (1981), "F Region East-West Drifts at Jicamarca," J. Geophys. Res., 86 (A1), 215-218.

Fremouw, E. J. (1980), "Geometrical Control of the Ratio of Intensity and Phase Scintillation Indices," J. Atm. Ter. Phys., 42, (9/10), 775.

Fremouw, E.J. (1983), "HiLat: A Pre-Launch Overview," DNA Report TR-81-276, Contract DNA001-81-C-0189, Physical Dynamics, Inc., Bellevue, WA.

Fremouw, E.J. and J.M. Lansinger (1981), "A Computer Model for High-Latitude Phase Scintillation Based on Wideband Satellite Data from Poker Flat," DNA Report 5686F, Contract DNA001-79-C-0372, Physical Dynamics, Inc., Bellevue, WA.

Fremouw, E J., R.L. Leadabrand, R.C. Livingston, M.D. Cousins, C.L. Rino, B.C. Fair, and R.A. Long (1978), "Early Results from the DNA Wideband Satellite Experiment - Complex-signal Scintillation," Rad. Sci., 13 (1), 167-187.

Fremouw, E. J., R. C. Livingston, and D. A. Miller (1980), "On the Statistics of Scintillating Signals," J. Atmos. Terr. Phys., 42, 717-731.

Fremouw, E.J., and D.A. Miller (1978), "Statistical Behavior of Signals from the Wideband Satellite," DNA Report 4818F, Contract DNA001-78-C-0042, Physical Dynamics Inc., Bellevue, WA.

Fremouw, E. J., C. L. Rino, R. C. Livingston, and M. C. Cousins (1977), "A Persistent Subauroral Scintillation Enhancement Observed in Alaska," Geophys. Res. Ltrs., 4 (11), 539

Heelis, R.A., J.K. Lowell, and R.W. Spiro (1982), "A Model of the Height-Latitude Ionospheric Convection Pattern," J. Geophys. Res., 87 (A8), 6339-6345.

Koster, J.R. (1958), "Radio Star Scintillations at an Equatorial Station," J. Atmos. Terr. Phys., 12, 100-109.

Koster, J.R. (1968), Equatorial Studies of the VHF Signal Radiated by Intelsat II, F-3: 1. Ionospheric Scintillation," Progress Report No. 3, Contract No. F61052-67-C-0027, University of Ghana-Legon, Accra, Ghana.

Koster, J. R., I. Katsriku, and M. Tete (1966), "Studies of the Equatorial Ionosphere Using Transmission from Active Satellites," Annual Summary Report 1, Contract AF61(052)-800, University of Ghana-Legon, Accra, Ghana.

Koster, J.R. and R.W. Wright (1960), "Scintillation, Spread F, and Transequatorial Scatter," J. Geophys. Res., 65(8), 2303.

Livingston, R. C., C. L. Rino, J. P. McClure, and W. B. Hanson (1981), "Spectral Characteristics of Medium-Scale Equatorial F-Region Irregularities," J. Geophys. Res., 86 (A4).

Maruyama, T. and N. Matuura (1984), "Longitudinal Variability of Annual Changes in Activity of Equatorial Spread F and Plasma Bubbles," J. Geophys. Res., 89 (A12), 10,903-10,912.

Moorthy, K. K., Reddi, C.R., and B.V.K. Murthy (1979), "Night-time Ionospheric Scintillations at the Magnetic Equator," J. Atmos. Terr. Phys., 41, 123-134.

Mullen, J.P., E. MacKenzie, and S. Basu (1984), "UHF/GHz Scintillation Observed at Ascension Island from 1980 Through 1982," Proceedings 1984 Symposium on the Effect of the Ionosphere on C^3 Systems, 1 -3 May 1984.

Paulson, M.R. (1979), "Scintillation of UHF SATCOM Signals," prepared for Naval Electron Systems Command by Naval Ocean System Center, NOSC Report No. 446.

Paulson, M.R. (1981), "Scintillation of VHF/UHF and L Band Satellite Signals at Guam," Rad. Sci., 16(15), 877-884.

Rastogi, R.G. and J. Mullen (1981), "Intense Daytime Radio Wave Scintillations and Sporadic E Layer Near the Dip Equator," J. Geophys. Res., 86 (A1), 195-198.

Rino, C. L. (1979a), "A Power Law Phase Screen Model for Ionospheric Scintillation. 1. Weak Scatter," Rad. Sci., 14 (6), 1135.

Rino, C.L. (1979b), "A Power Law Phase Screen Model for Ionospheric Scintillation. 2. Strong Scatter," Rad. Sci., 14 (6), 1147.

Rino, C.L. and E.J. Fremouw (1977), "The Angle Dependence of Singly Scattered Wavefields," J. Atmos. and Terr. Phys., 39, 859.

Rino, C.L., E.J. Fremouw, R.C. Livingston, M.D. Cousins, and B.C. Fair (1977), "Wideband Satellite Observations," DNA Report 4399F, Contract DNA001-75-C-0111, SRI International, Menlo Park, CA.

Rino, C.L. and R.C. Livingston (1982), "On the Analysis and Interpretation of Spaced-Receiver Measurements of Transionospheric Radio Waves," Radio Science, 17 (4), 845-854.

Rino, C. L., R. C. Livingston, and S. J. Matthews (1978), "Evidence for Sheetlike Auroral Ionospheric Irregularities," Geophys. Res. Ltrs., 5 (12), 1039.

Rino, C.L., R.T. Tsunoda, J. Petriceks, R.C. Livingston, M.C. Kelley, and K.D. Baker (1981), "Simultaneous Rocket-borne Beacon and In-situ Measurements of Equatorial Spread F - Intermediate Wavelength Results," J. Geophys. Res., 86, (A4), 2411-2420.

Rumsey, V. H. (1975), "Scintillations Due to a Concentrated Layer With a Power-Law Turbulence Spectrum," Rad. Sci., 10 (1), 107-114.

Secan, J.A. and E.J. Fremouw (1983a), "Improvement of the Scintillation-Irregularity Model in WBMOD," DNA Report TR-81-241, Contract DNA001-81-C-0092, Physical Dynamics, Inc., Bellevue, WA.

Secan J.A. E.J. Fremouw (1983b), "Improvements in Operational Codes Describing the Ambient Ionosphere," Defense Nuclear Agency, Progress Report No. 2, Contract DNA001-83-C-0097, Physical Dynamics, Inc., Bellevue, WA.

Tsunoda, R.T. (1985), "Control of the Seasonal and Longitudinal Occurrence of Equatorial Scintillations by the Longitudinal Gradient in Integrated E Region Pedersen Conductivity," J. Geophys. Res., 90 (A1), 447-456.

VanZandt, T.E., W.L. Clark, and J.M. Warnick (1972), "Magnetic Apex Coordinates: A Magnetic Coordinate System for the Ionospheric F2 Layer," J. Geophys. Res., 77, 2406.

DISTRIBUTION LIST

DEPARTMENT OF DEFENSE

DEFENSE INTELLIGENCE AGENCY
    ATTN: RTS-2B

DEFENSE NUCLEAR AGENCY
    ATTN: NATF
    ATTN: NAWE
3 CYS ATTN: RAAE
    ATTN: RAAE P LUNN
    ATTN: RAEE
    ATTN: STNA
4 CYS ATTN: STTI-CA

DEFENSE TECHNICAL INFORMATION CENTER
12 CYS ATTN: DD

DEPARTMENT OF THE ARMY

BMD ADVANCED TECHNOLOGY CENTER
    ATTN: ATC-R D RUSS
    ATTN: ATC-R W DICKSON

U S ARMY COMMUNICATIONS R&D COMMAND
    ATTN: DRDCO-COM-RY W KESSELMAN

U S ARMY NUCLEAR & CHEMICAL AGENCY
    ATTN: LIBRARY

U S ARMY SATELLITE COMM AGENCY
    ATTN: DOCUMENT CONTROL

DEPARTMENT OF THE NAVY

NAVAL RESEARCH LABORATORY
    ATTN: CODE 4180 J GOODMAN
    ATTN: CODE 4187
    ATTN: CODE 4706 P RODRIGUEZ
    ATTN: CODE 4720 J DAVIS

NAVAL TELECOMMUNICATIONS COMMAND
    ATTN: CODE 341

SPACE & NAVAL WARFARE SYSTEMS CMD
    ATTN: CODE 3101 T HUGHES
    ATTN: CODE 501A
    ATTN: PDE-110-X1 B KRUGER
    ATTN: PDE-110-11021 G BRUNHART
    ATTN: PME 106-4 S KEARNEY
    ATTN: PME 117-20
    ATTN: PME-106 F W DIEDERICH

STRATEGIC SYSTEMS PROGRAMS (PM-1)
    ATTN: NSP-2141
    ATTN: NSP-2722
    ATTN: NSP-43 TECH LIB

THEATER NUCLEAR WARFARE PROGRAM OFC
    ATTN: PMS-423 D SMITH

DEPARTMENT OF THE AIR FORCE

AIR FORCE GEOPHYSICS LABORATORY
    ATTN: CA A STAIR
    ATTN: LID J RAMUSSEN
    ATTN: LIS J BUCHAU
    ATTN: LS
    ATTN: LS R O'NIEL
    ATTN: LYD K CHAMPION

AIR FORCE WEAPONS LABORATORY, AFSC
    ATTN: NTN
    ATTN: SUL

AIR FORCE WRIGHT AERONAUTICAL LAB/AAAD
    ATTN: A JOHNSON
    ATTN: W HUNT

DEPARTMENT OF ENERGY

LOS ALAMOS NATIONAL LABORATORY
    ATTN: D SAPPENFIELD

SANDIA NATIONAL LABORATORIES
    ATTN: D HARTLEY 8300
    ATTN: T COOK

SANDIA NATIONAL LABORATORIES
    ATTN: D DAHLGREN
    ATTN: D THORNBROUGH
    ATTN: ORG 1231 R C BACKSTROM
    ATTN: ORG 1250 W BROWN
    ATTN: SPACE PROJECT DIV
    ATTN: TECH LIB 3141

DEPARTMENT OF DEFENSE CONTRACTORS

AEROSPACE CORP
    ATTN: D OLSEN
    ATTN: I GARFUNKEL
    ATTN: J KLUCK
    ATTN: J STRAUS
    ATTN: K S CHO
    ATTN: R SLAUGHTER
    ATTN: T SALMI
    ATTN: V JOSEPHSON

AUSTIN RESEARCH ASSOCIATES
    ATTN: J THOMPSON

BERKELEY RSCH ASSOCIATES, INC
    ATTN: J WORKMAN
    ATTN: S BRECHT

DEPT OF DEFENSE CONTRACTORS (CONTINUED)

EOS TECHNOLOGIES, INC
    ATTN: B GABBARD
    ATTN: W LELEVIER

JAYCOR
    ATTN: J SPERLING

JOHNS HOPKINS UNIVERSITY
    ATTN: C MENG
    ATTN: J D PHILLIPS
    ATTN: J NEWLAND
    ATTN: K POTOCKI
    ATTN: R STOKES
    ATTN: T EVANS

KAMAN TEMPO
    ATTN: B GAMBILL
    ATTN: DASIAC

KAMAN TEMPO
    ATTN: DASIAC

MAXIM TECHNOLOGIES, INC
    ATTN: J MARSHALL
    ATTN: R MORGANSTERN

MISSION RESEARCH CORP
    ATTN: C LAUER
    ATTN: D KNEPP
    ATTN: F FAJEN
    ATTN: F GUIGLIANO
    ATTN: G MCCARTOR
    ATTN: R BIGONI
    ATTN: R BOGUSCH
    ATTN: R DANA
    ATTN: R HENDRICK
    ATTN: S GUTSCHE
    ATTN: TECH LIBRARY

PACIFIC-SIERRA RESEARCH CORP
    ATTN: H BRODE, CHAIRMAN SAGE

PHYSICAL DYNAMICS, INC
2 CYS ATTN: E FREMOUW
2 CYS ATTN: R ROBINS

PHYSICAL RESEARCH, INC
    ATTN: R DELIBERIS
    ATTN: T STEPHENS

PHYSICAL RESEARCH, INC
    ATTN: J DEVORE
    ATTN: J THOMPSON
    ATTN: W SCHLUETER

R & D ASSOCIATES
    ATTN: B MOLLER
    ATTN: C GREIFINGER
    ATTN: F GILMORE
    ATTN: G STCYR
    ATTN: H ORY
    ATTN: M GANTSWEG
    ATTN: M GROVER
    ATTN: P HAAS
    ATTN: R TURCO
    ATTN: W KARZAS

SCIENCE APPLICATIONS INTL CORP
    ATTN: C SMITH
    ATTN: D HAMLIN
    ATTN: E STRAKER
    ATTN: L LINSON

SRI INTERNATIONAL
    ATTN: C RINO
    ATTN: D NIELSON
    ATTN: G PRICE
    ATTN: G SMITH
    ATTN: R LEADABRAND
    ATTN: R LIVINGSTON
    ATTN: R TSUNODA
2 CYS ATTN: W CHESNUT
    ATTN: W JAYE

TOYON RESEARCH CORP
    ATTN: J GARBARINO
    ATTN: J ISE

VISIDYNE, INC
    ATTN: J CARPENTER